Polarimetric Observations and Simulations of Sublimating Snow: Implications for Nowcasting

JACOB T. CARLIN,[a,b] HEATHER D. REEVES,[a,b] AND ALEXANDER V. RYZHKOV[a,b]

[a] *Cooperative Institute for Mesoscale Meteorological Studies, University of Oklahoma, Norman, Oklahoma*
[b] *NOAA/OAR National Severe Storms Laboratory, Norman, Oklahoma*

(Manuscript received 1 March 2021, in final form 23 June 2021)

ABSTRACT: Snow sublimating in dry air is a forecasting challenge and can delay the onset of surface snowfall and affect storm-total accumulations. Despite this fact, it remains comparatively less studied than other microphysical processes. Herein, the characteristics of sublimating snow and the potential for nowcasting snowfall reaching the surface are explored through the use of dual-polarization radar. Twelve cases featuring prolific sublimation were analyzed using range-defined quasi-vertical profiles (RDQVPs) and were compared with environmental model analyses. Overall, reflectivity Z significantly decreases, differential reflectivity Z_{DR} slightly decreases, and copolar-correlation coefficient ρ_{hv} remains nearly constant through the sublimation layer. Regions of enhanced specific differential phase K_{dp} were frequently observed in the sublimation layer and are believed to be polarimetric evidence of secondary ice production via sublimation. A 1D bin model was initialized using particle size distributions retrieved from the RDQVPs using numerous novel polarimetric snow retrieval relations for a wide range of forecast lead times, with the model environment evolving in response to sublimation. It was found that the model was largely able to predict the snowfall start time up to 6 h in advance, with a 6-h median bias of just −18.5 min. A more detailed case study of the 8 December 2013 snowstorm in the Philadelphia, Pennsylvania, region was also performed, demonstrating good correspondence with observations and examples of model fields (e.g., cooling rate) hypothetically available from such a tool. The proof-of-concept results herein demonstrate the potential benefits of incorporating spatially averaged radar data in conjunction with simple 1D models into the nowcasting process.

SIGNIFICANCE STATEMENT: The goals of this work are to comprehensively survey the dual-polarization radar characteristics of snow evaporating in dry air and to investigate whether information gleaned from polarimetric radars can be used with a predictive model to help make short-term predictions about when snow will overcome dry air and reach the ground. We found that by using this radar information and a simple model we could predict the start time of snow up to 6 h in advance with reasonable accuracy. In conjunction with other available data, this proof of concept could help forecasters to make short-term predictions about when snowfall impacts will begin.

KEYWORDS: Snow; Winter/cool season; Cloud microphysics; Latent heating/cooling; Sublimation; Radars/Radar observations; Nowcasting; Single column models

1. Introduction

Winter precipitation presents a number of societal hazards including increased risk of pedestrian, vehicular, and aviation accidents (e.g., Qiu and Nixon 2008; Black and Mote 2015a,b; Mills et al. 2020) and significant economic losses (e.g., Lazo et al. 2020). Despite steady improvement in numerical weather prediction (NWP) skill over the past few decades (Bauer et al. 2015), the prediction of winter precipitation, including snow, remains a primary forecasting challenge as it is often the result of interactions among many intricate processes, both microphysical and dynamical.

Herein, the focus is on the effects of sublimation on the timing and intensity of snow. At first glance, sublimation may seem less consequential than the much-more-studied effects of melting and evaporation (e.g., Wexler et al. 1954; Homan and Uccellini 1987; Szeto and Stewart 1997; Gallus and Segal 1999; Kain et al. 2000; Frick and Wernli 2012). However, sublimation can have a complex range of effects. First, owing to the large enthalpy of sublimation and the relatively slow terminal velocity of snowflakes, sublimation may rapidly cool and moisten dry environments, allowing snow to reach the surface unexpectedly (Market et al. 2006). In addition, this cooling can force a dynamic response that promotes frontogenesis and generates convective instability and/or turbulence below cloud base, all of which can have a positive feedback on the production of snow (e.g., Harris 1977; Auria and Campistron 1987; Clough and Franks 1991; Parker and Thorpe 1995; Clough et al. 2000; Kudo 2013; Kudo et al. 2015; Kantha et al. 2019). Sublimation has also been proposed as a possible secondary ice production (SIP) mechanism for dendritic and irregularly shaped ice crystals (e.g., Oraltay and Hallett 1989; Korolev et al. 2020), as sublimation diminishes and weakens the supporting structure of the narrow branches and subbranches and makes them more prone to fracturing. Thus, because sublimation often precedes snow reaching the surface through antecedent dry air, determining the rate at which this dry air is eroded is crucial for accurately predicting both the onset of snow and storm-total accumulations. Prediction of sublimation has received limited attention in the literature. Forbes and Hogan (2006) examined the ability of NWP models to accurately simulate sublimation rates. They found that, relative to ice water content (IWC) estimated from radar

Corresponding author: Jacob T. Carlin, jacob.carlin@noaa.gov

DOI: 10.1175/JAMC-D-21-0038.1

reflectivity Z, the model systematically underpredicted IWC but overpredicted sublimation depths (defined as the depth over which a 90% reduction in IWC occurred) by over 250%, resulting in a severe underestimation of the cooling rate due to sublimation by an order of magnitude. This discrepancy was hypothesized to be due to improper particle fall speed parameterizations, insufficient vertical grid spacing, or a moist bias in the model, but it demonstrates clearly the challenge of accurately simulating the erosion of dry air by snow and the sort of information radar data may be able to provide.

A potentially useful tool for improving sublimation nowcasting are dual-polarization radars. These have become an integral tool for studying ice microphysics as they provide information about particles' phase, shape, orientation, and concentration. Such studies have yielded insights on a variety of ice microphysical processes including deposition, aggregation, melting, riming, and rime splintering (e.g., Giangrande et al. 2008; Kennedy and Rutledge 2011; Andrić et al. 2013; Schneebeli et al. 2013; Trömel et al. 2014; Grazioli et al. 2015; Leinonen and Szyrmer 2015; Li et al. 2018; Moisseev et al. 2015; Schrom et al. 2015; Wolfensberger et al. 2016; Sinclair et al. 2016; Griffin et al. 2018; Carlin and Ryzhkov 2019; Griffin et al. 2020; Schrom et al. 2021). Improved understanding of how polarimetric signatures relate to precipitation processes is beginning to lead to exploration of polarimetric radar nowcasting applications. For example, periods of enhanced specific differential phase K_{dp} observed in the dendritic growth layer indicative of increased concentrations and/or growth of ice crystals (e.g., Kennedy and Rutledge 2011) have been shown to reliably precede increased rain rates at the surface by up to 120 min (Bechini et al. 2013; Trömel et al. 2019). These findings serve as proofs of concept for using polarimetric radar observations aloft to make inferences about impending conditions at the surface. Similarly, Tobin and Kumjian (2017) demonstrated that under constant warm air advection, polarimetric refreezing-layer signatures aloft can be extrapolated to the surface to nowcast the ice-pellet–freezing-rain transition time. However, few polarimetric radar studies have been devoted to sublimation. Using lidar and polarimetric radar observations, Westbrook et al. (2010) concluded that sublimating pristine ice crystals maintain their horizontal orientations despite cooling-induced turbulence. Sulia and Kumjian (2017) used the density- and shape-varying adaptive-habit model (Sulia and Harrington 2011; Harrington et al. 2013) to simulate the polarimetric variables of Arctic ice crystals and found an overall decrease in Z and differential reflectivity Z_{DR} during sublimation as aspect ratios were assumed to tend toward unity.

In this paper we examine polarimetric observations of sublimating snow, and whether a simple 1D model initialized from these observations can be used to nowcast the start time of snow at the surface. Section 2 details how cases were selected and the observed polarimetric characteristics of sublimating snow, and section 3 presents the model, method, and nowcasting simulation results. A discussion of caveats, sensitivities, and future work follows in section 4, followed by a summary of findings in section 5.

TABLE 1. Details of selected cases.

Date	Times (UTC)	Radar site
5–6 Nov 2013	1500–0300	Minneapolis, MN (KMPX)
7–8 Dec 2013	1800–0200	Hastings, NE (KUEX)
8–9 Dec 2013	1200–0000	Philadelphia, PA (KDIX)
20 Jan 2016	0800–2000	Cleveland, OH (KCLE)
22 Dec 2017	0600–1800	Portland, ME (KGYX)
3–4 Jan 2018	1400–0200	Raleigh, NC (KRAX)
8–9 Nov 2018	1800–0600	Saint Louis, MO (KLSX)
18–19 Jan 2019	1800–0600	Grand Rapids, MI (KGRR)
20 Feb 2019	1000–2200	Chicago, IL (KLOT)
12–13 Feb 2019	1500–0300	Portland, ME (KGYX)
11–12 Dec 2019	2300–1100	Duluth, MN (KDLH)
17–18 Jan 2020	1400–0000	Milwaukee, WI (KMKX)

2. Polarimetric observations of sublimation

a. *Case selection and data processing*

To find cases of dry air impeding snow from reaching the surface that were of operational concern, historical Area Forecast Discussions (AFDs) from Central and Eastern Region National Weather Service (NWS) offices were searched during the polarimetric WSR-88D era (2013–present) from November through April. An algorithm was used to search archived AFDs and identify those that contained either the words "dry," "snow," and "sublimate/sublimation/sublimating," or "snow" and "donut," the latter being an oft-used colloquialism for a ring of Z surrounding the radar site reminiscent of the eponymous ring-shaped fried-dough confection; this ring is caused by the radar beam going from a snow-free layer to one containing snow as it ascends and is frequently observed during sublimation of horizontally homogeneous precipitation. Duplicates resulting from the reissuance of portions of AFDs and cases referring to sublimation of snow cover were then manually excluded. The remaining cases were subjectively reviewed to identify ones in which

1) snow was eventually observed at the surface,
2) minimal to no melting occurred, and
3) precipitation was widespread, sufficiently heavy, and relatively homogeneous (i.e., not lake-effect snow or convective snow showers), with a clear descent of snow toward the ground around the radar,

in an attempt to isolate the impacts of sublimational cooling/moistening. A total of 12 cases were selected that met these criteria while still reflecting a diversity of geographic locations, synoptic-scale meteorological conditions, and temperature ranges. These cases are summarized in Table 1.

Polarimetric range-defined quasi-vertical profiles (RDQVPs; Tobin and Kumjian 2017) were created for each case using a 50-km radius. The polarimetric characteristics of aggregated snow (of which we believe most of these cases are primarily composed) are muted because of their low density and large diversity of orientations, with observations exhibiting an appreciable amount of noise relative to the intrinsic values. However, the azimuthal averaging performed when generating RDQVPs greatly reduces this noise and allows for a more

granular look at the changes of each polarimetric variable. The K_{dp} was calculated from differential phase shift Φ_{dp} prior to azimuthal averaging according to the following procedure. Filtering was performed by applying a sliding-window five-gate mean filter three times and then removing regions of Φ_{dp} where the standard deviation around this smoothed mean in a nine-gate moving window exceeded 10° or where the copolar-correlation coefficient ρ_{hv} dropped below 0.6. An additional five-gate median filter and nine-gate moving average were subsequently applied. The K_{dp} was calculated as one-half of the slope of a least squares fit on this smoothed Φ_{dp} profile using a 25-gate window. No calibration for Z or Z_{DR} was performed prior to computing the RDQVPs. In many of the cases, discontinuous bands with abrupt shifts in median values were observed in the initial RDQVPs on the underside of the more-homogeneous precipitation shield due to small, localized areas of heavier precipitation reaching farther into the dry layer. These bands were identified using a vertical gradient threshold-based approach and removed from each of the RDQVPs to retain the more representative precipitation regions.

Figure 1 shows the RDQVPs of Z, with contours of relative humidity with respect to ice (RH_i) from the corresponding Rapid Refresh (RAP; Benjamin et al. 2016) model analyses at the nearest model grid point to the radar site overlaid. A cursory comparison between the RAP RH_i profiles and RH_i from observed sounding data for the two cases with collocated sounding sites available at relevant times (0000 UTC 6 November 2013 at KMPX and 1200 UTC 22 December 2017 at KGYX) showed good agreement. All of the cases have an antecedent dry layer that typically stretches from approximately 1 km AGL to as high as 5–6 km AGL with minimum RH_i values frequently below 10%. These layers gradually erode (demonstrated by the bending and descent of high-RH_i contours toward the surface over time, e.g., Fig. 1d) as sublimation cools and moistens the air and nonnegligible Z descends toward the ground in a manner that is typically, but not always, monotonic. Overall, the analyzed RH_i fields show relatively good agreement with the Z fields, with the last layers of substantially dry air eroding around the time that nonnegligible Z reaches the surface.

b. Analysis

The bulk polarimetric characteristics of sublimating snow were analyzed for each of the 12 cases. The top of the sublimation layer was defined as the point where Z first decreased to 90% of its maximum value in the column in order to avoid highly variable height estimates due to minor changes in Z; the bottom of the layer was either where Z reached −10 dBZ or valid data ceased. RDQVP columns (i.e., radar scans) were included until the point in time that Z of at least 0 dBZ reached the surface. The choice of −10 dBZ is an admittedly subjective threshold, but it seems a reasonable choice for ensuring sufficient signal in an RDQVP context; additionally, the Z often increases rapidly once it reaches the surface, making the results fairly insensitive to the exact surface snowfall threshold chosen. The determined sublimation layers are shown in Fig. 1. For each volume scan, the vertical profiles of the observed polarimetric variables within the identified sublimation layer were normalized to a common relative depth (i.e., the profiles were stretched or compressed so that the top and bottom of each scan's sublimation layer were at the same relative height) prior to computing the median to more clearly show the overall trend of each variable throughout the sublimation layer. Variability in the nonnormalized top and bottom of the sublimation layer caused a varying number of radar scans to be included in the median calculation at each height and, subsequently, noisy profiles that were often not meaningful and unrepresentative of what could be gleaned from the RDQVP (e.g., combining profiles at the bottom of some sublimation layers with the middle of others), making such a normalization necessary. Additionally, the calculated changes of the polarimetric radar variables between the top and bottom of the sublimation layer are not true Lagrangian estimates of a population of particles undergoing sublimation; the differences are taken between different heights within a given volume scan (i.e., at the same time) with no fall speed considerations included. We believe this assumption to be acceptable if the precipitation characteristics evolve gradually, which was generally the case, as there is no clear way to account for the influence of fall speed variability from the RDQVP data. In some cases, fallstreaks were observed (e.g., Figs. 1a,c,e,j), seemingly violating the assumptions behind this approach. We explored ways to correct for or otherwise remove such fallstreaks, but such attempts proved difficult and required additional complicating and potentially problematic assumptions. However, many of the most prominent fallstreaks were during the heaviest precipitation after snow had reached the surface and were thus not included. Additionally, the impact of the time lag induced by these fallstreaks is diminished when only examining the narrow sublimation layer (e.g., for a 500-m-deep sublimation layer and a terminal velocity of 1.0 m s^{-1}, the particle residence time is about 1–2 radar volumes, depending on the chosen scanning strategy). Finally, the transitory nature of the fallstreaks results in compensating biases on either side of the fallstreak, which should have minimal impact on the resultant median values for an entire case. With these caveats in mind, we believe such analysis to still be worthwhile and informative.

Figure 2 shows the median vertical profiles of Z, Z_{DR}, ρ_{hv}, and K_{dp} through the sublimation layer for each of the 12 cases, along with their median absolute deviations (MADs). The MAD is an outlier-resistant measure of spread defined by (Wilks 2011; Leys et al. 2013)

$$\mathrm{MAD} = \mathrm{median}(|x_i - q_{0.5}|), \tag{1}$$

where x_i is each data point in the population and $q_{0.5}$ is the median of the population. The Z for all cases decreases through the sublimation layer, decreasing more rapidly toward the bottom of the layer (Fig. 2a). This decrease was anticipated as particle sizes monotonically decrease while sublimating and the ice water content tends toward zero. Figure 3 shows the distribution of the change in Z, Z_{DR}, and K_{dp} between the top and bottom of the sublimation layer for all scans of each case to show the variability around the median within each case. The median decrease in Z across all cases ranged from 5 to 22 dB, with an average decrease of approximately 15 dB. The cases

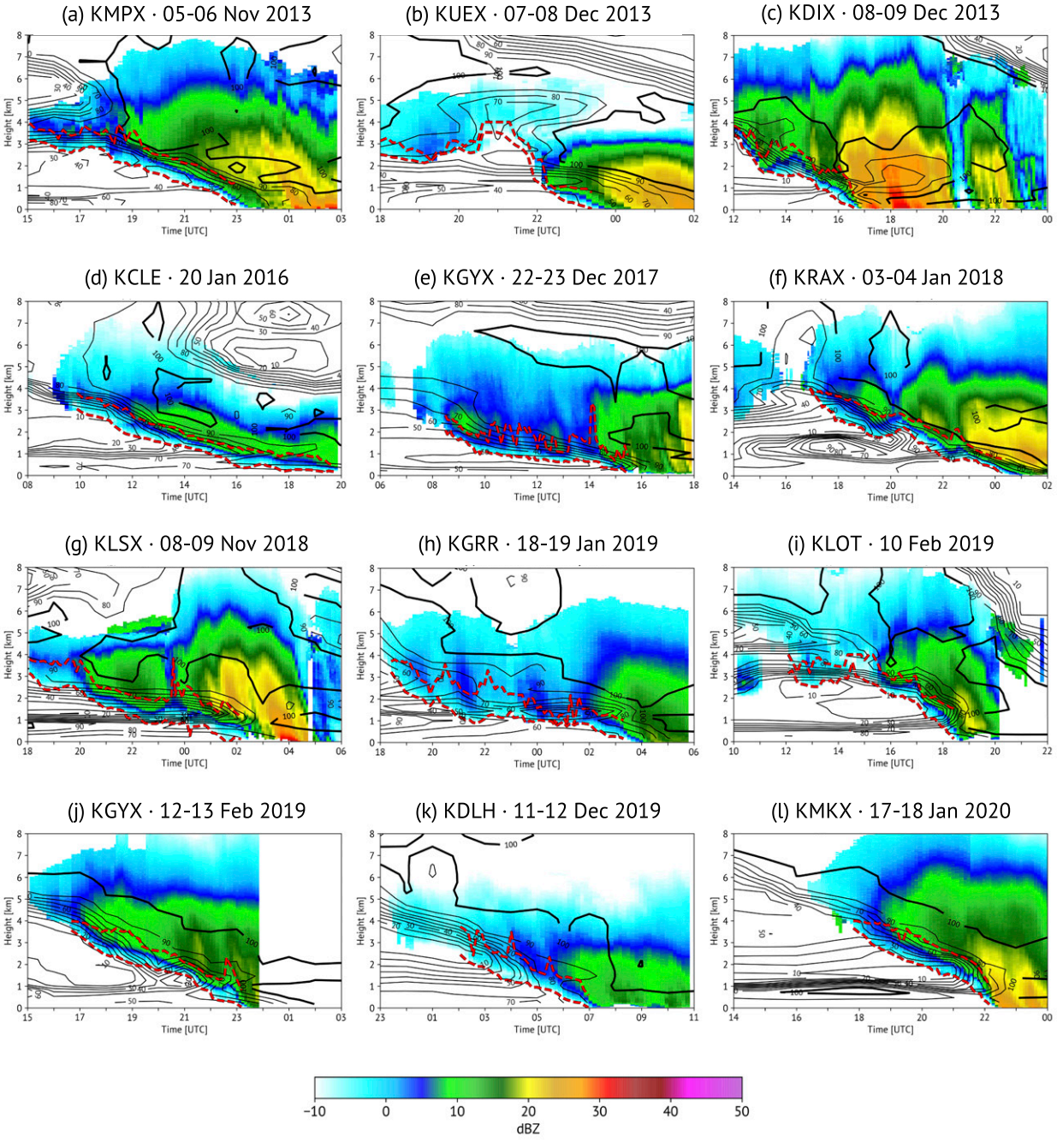

FIG. 1. RDQVPs of Z for selected cases (color shades). Contours of RH_i from the corresponding hourly RAP analyses are shown in black (contoured every 10%), with 100% highlighted. The identified sublimation layer is denoted between the two red dashed lines.

with the broadest ΔZ distributions are those that appreciably intensified during the sublimation period. The Z MAD (Fig. 2a), which measures the spread of Z at a given height within the sublimation layer, generally remains less than 5 dB and decreases downward, similarly reflecting the general variability of precipitation intensity at the top of the sublimation layer over each system's life cycle during the examined periods. The only exception to this is a slight increase in MAD near the bottom of the sublimation layer, which reflects spread caused by terminating the profiles at either −10 dBZ or the lowest usable data.

The median profiles Z_{DR}, on the other hand, decrease at a nearly constant rate for most cases (Fig. 2b) and exhibit relatively small changes, with an average median decrease through

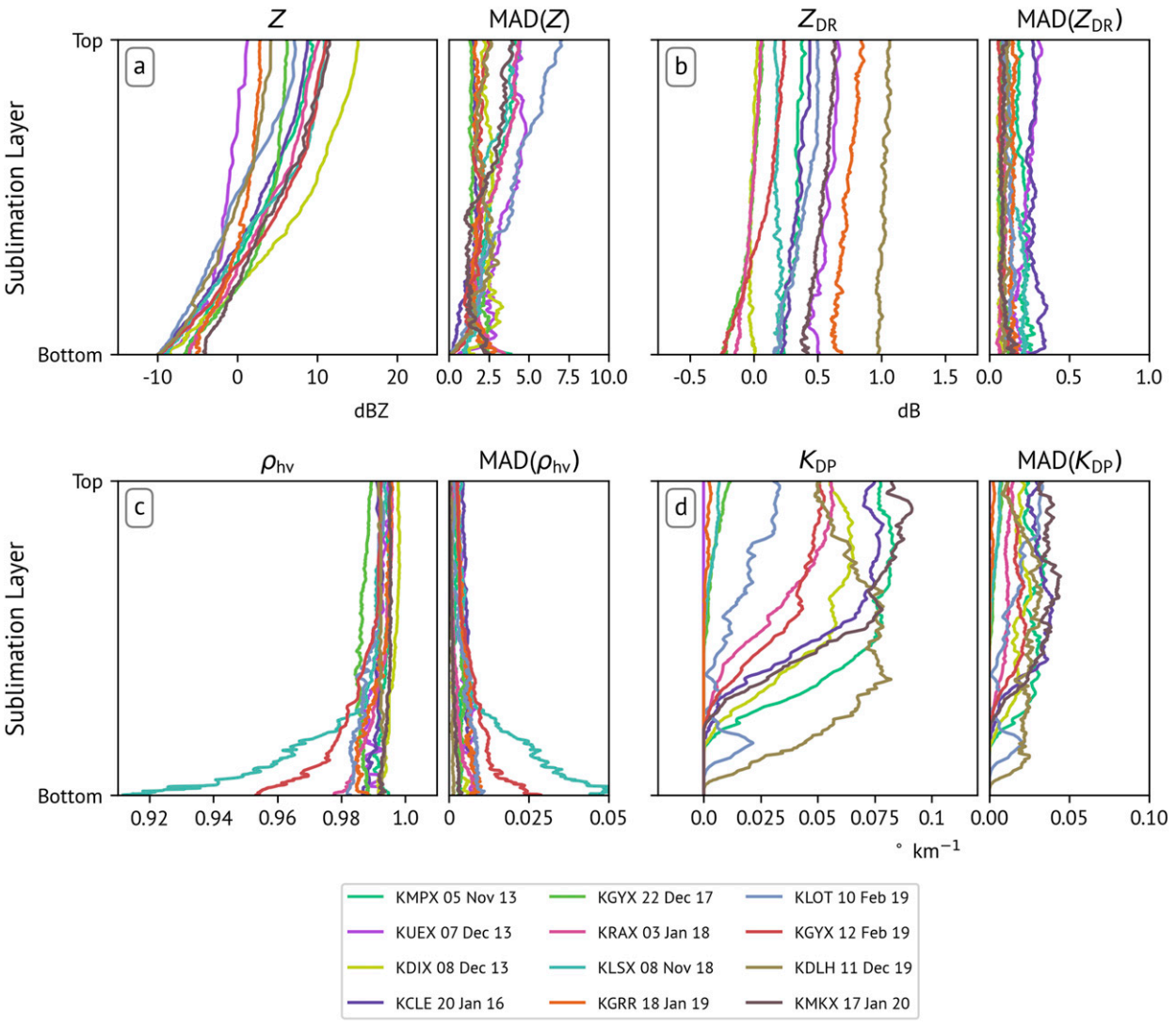

FIG. 2. Median normalized vertical profiles of (a) Z, (b) Z_{DR}, (c) ρ_{hv}, and (d) K_{dp} and their MAD (Wilks 2011) through the sublimation layer for each case.

the sublimation layer of 0.19 dB (Fig. 3b). However, variability in these median values between cases exists, with a maximum decrease of nearly 0.5 dB for KGYX on 12 February 2019 and a minimum decrease of just 0.06 dB for KDLH on 11 December 2019. While most of the distributions are relatively narrow, a few of the cases exhibit long tails. Negative tails (e.g., KMPX on 5 November 2013 and KGRR on 18 January 2019) are associated with periods of very large Z_{DR} of 1.0–4.0 dB and small Z values indicative of sparse, pristine ice crystals, although in the latter case the gradient appears to be exacerbated by fallstreaks associated with the generation and slow terminal velocity of pristine crystals aloft. A few cases (e.g., KUEX 7 on December 2013 and KLSX on 8 November 2018) also exhibit positive tails associated with brief periods of localized Z_{DR} enhancements near the base of the sublimation layer. However, the distribution tails of even these cases represent a small fraction of the observed profiles; the Z_{DR} MAD (Fig. 2b) profiles for nearly all cases remain steady and less than 0.25 dB at all heights, indicating a fair degree of consistency throughout most of the event periods.

There are a number of potential causes of these overall Z_{DR} decreases. Past studies of in situ measurements, wind tunnel experiments, and simulations all indicate that sublimation of pristine ice crystals in substantially subsaturated air tends to result in a *rounding* of the faceted edges of pristine ice crystals (Nelson 1998; Bacon et al. 1998; Korolev et al. 1999; Dominé et al. 2003; Westbrook et al. 2010; Korolev et al. 2017; Jambon-Puillet et al. 2018; Voigtländer et al. 2018) that would tend to increase particles' resemblance to idealized spheroids and possibly reduce the near-field interactions of branched crystals that can result in Z_{DR} enhancements (Schrom and Kumjian 2018). However, Nelson (1998) found that these changes did not appreciably affect the overall particle aspect ratio, which remained nearly constant during sublimation for the individual

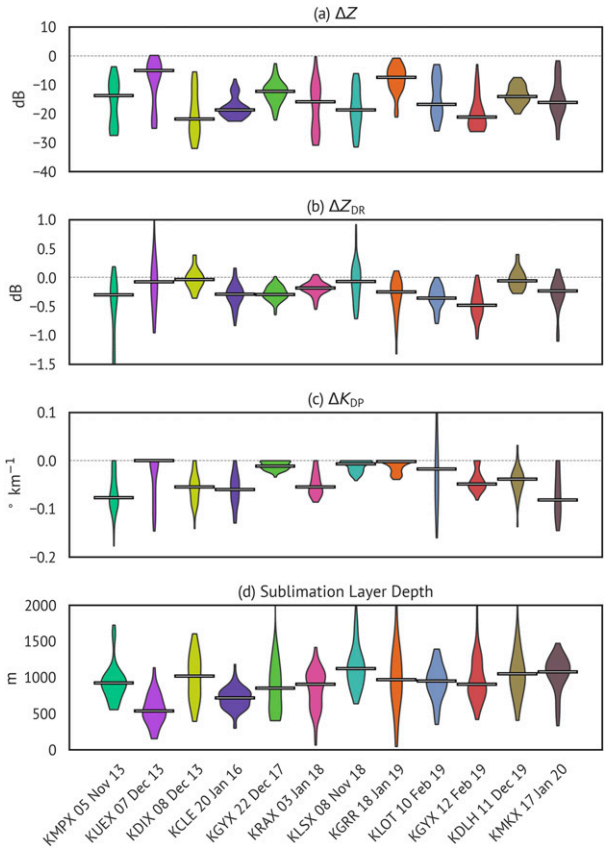

FIG. 3. Violin plots of the change in (a) Z, (b) Z_{DR}, and (c) K_{dp} between the top and bottom of the sublimation layer and (d) the depth of the sublimation layer for each case. Distribution medians are denoted by the thick horizontal bars.

crystals examined. This is in contrast to the assertion that sublimation acts in the opposite manner as depositional growth (e.g., Pruppacher and Klett 1997), which would result in increasingly spherical particles during sublimation. Separate from changes in shape, increased turbulence due to cooling within the sublimation layer might also act to broaden the canting angle distribution of particles and decrease the overall measured Z_{DR}. Many theoretical (e.g., Klett 1995, and references therein) and observational (Westbrook et al. 2010) studies have concluded that the velocity fluctuations imposed on particles by turbulent eddies at scales comparable to their size are insufficient to cause appreciable canting. However, other studies (Kantha et al. 2019) have reported eddy dissipation rates beneath sublimating snow up to three orders of magnitude higher than those observed in Westbrook et al. (2010). Garrett et al. (2015) also reported increasingly broad snowflake canting angle distributions with increasing turbulence, although uncertainty remains as disturbance of particle orientations due to turbulence generated by the sensor cannot be ruled out (Jiang et al. 2019). For the majority of profiles believed to be composed primarily of aggregates, supporting evidence for the impact of changing shapes is obfuscated by their extremely low densities, which mutes the response of Z_{DR} to changes in aspect ratio. In addition, for mixtures of pristine crystals and aggregates, smaller, denser particles that are more anisotropic sublimate completely first, resulting in an increase in the mean aspect ratio and decrease in the particle effective density, both of which would decrease the overall Z_{DR}. This vertical gradient in particle characteristics would also be exacerbated by size sorting due to differential fall speeds.

The ρ_{hv} profiles generally remain above 0.98 with a slight decrease toward the bottom of the sublimation layer (Fig. 2c). The only exceptions are on 8 November 2018 at KLSX, which briefly began as rain and therefore features some brightband contamination, and 12 February 2019 at KGYX, for which the reductions in ρ_{hv} appear to be a consequence of azimuthally variable extensions of weak precipitation into the sublimation layer.

The K_{dp} profiles are also noteworthy. More than one-half of cases exhibit median values exceeding 0.05° km^{-1} through much of the sublimation layer before rapidly decreasing toward the bottom (Fig. 2d). This signature is examined in more detail in Fig. 4. The enhanced K_{dp} values are confined to coherent bands in the lowest portion of the precipitation that are distinct from any enhanced K_{dp} regions aloft. K_{dp} values in these bands occasionally approach 0.2° km^{-1} (e.g., Figs. 4a,d) and reached as high as 0.5° km^{-1} from 1500 to 1700 UTC 10 February 2019 at KLOT (Fig. 4i). The K_{dp} MAD (Fig. 2d) is also relatively higher than it is for other variables in comparison with the median K_{dp} values, indicative of the often transient and variable nature of these enhancements. The change in K_{dp} within the sublimation layer (Fig. 3c) also bears this out, with short, narrow distributions for the cases that did not exhibit this signature and relatively wide distributions for those that did. The only case to exhibit any positive net changes of K_{dp} was 10 February 2019 at KLOT; this was due to the brief but large increase in K_{dp} near the bottom of the sublimation layer between 1500 and 1700 UTC (Fig. 4i).

To ensure that the enhanced K_{dp} regions are not a result of noisy Φ_{dp} and boundary effects near the edge of the precipitation, individual rays of Φ_{dp} are examined during times of enhanced K_{dp} and are shown in Fig. 5. For both the KMPX and KCLE cases, there is a rapid and pronounced increase in Φ_{dp} of approximately 3°–4° within the Z gradient (at roughly gates 120–150), which then levels off before increasing again in the so-called dendritic growth layer (DGL; gates 225 onward) between −12 and −18°C, where the growth of planar crystals (e.g., plates and dendrites) is favored. While the individual rays of Φ_{dp} (Figs. 5a,c) are indeed quite noisy, as is typical, the increase is pronounced, and occurs even in regions of appreciable Z away from the immediate precipitation edge; in the KMPX case, the region of rapidly increasing Φ_{dp} actually exhibits some of the lowest variance around the smoothed Φ_{dp} of the entire ray. These trends are even more clear in the 30° sector averages (Figs. 5b,d), which exhibit markedly reduced noise due to the averaging. In both of these cases, the noisy Φ_{dp} between gates 50 and 100 gives way to a pronounced monotonic increase in Φ_{dp} before beginning to increase more gradually. Qualitatively similar trends were observed for other azimuths and cases examined (not shown). This sort of examination of the raw Φ_{dp} data provides confidence that this phase shift signal is not due to K_{dp} processing effects.

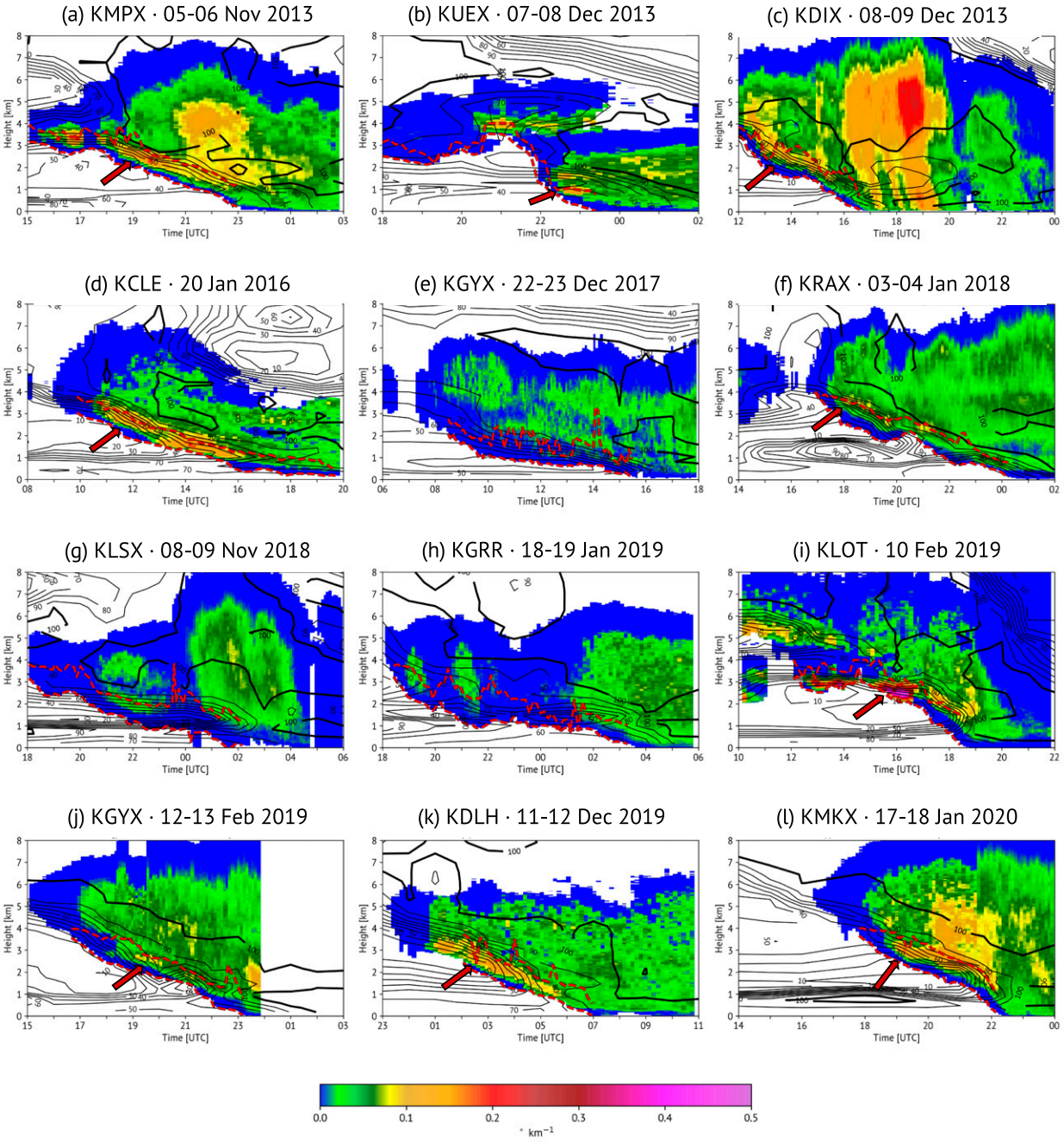

FIG. 4. As in Fig. 1, but for K_{dp} (° km^{-1}). Red arrows indicate regions of interest for possible secondary ice production.

In most of the cases exhibiting this signature, moderate Z and low Z_{DR} values suggest the prevalence of aggregates, which contribute negligibly to K_{dp}. Apart from the aforementioned DGL, where enhanced K_{dp} has been attributed to both highly oblate planar crystals (e.g., Kennedy and Rutledge 2011; Bechini et al. 2013; Schrom et al. 2015; Griffin et al. 2018) and/or large concentrations of more-isometric small, dense crystals (e.g., Schrom and Kumjian 2016; Griffin et al. 2018), enhanced regions of K_{dp} in areas of ice have also recently been attributed to SIP due to rime splintering (Grazioli et al. 2015; Kumjian et al. 2016; Sinclair et al. 2016; Kumjian and Lombardo 2017). However, the consistently subsaturated RH$_i$ in these regions preclude riming as an explanation.

Instead, we posit that these K_{dp} enhancements are evidence of SIP due to sublimation. This mechanism of SIP has received comparatively little attention, with some doubt expressed about its significance for further ice multiplication and/or seeding due to the subsequent rapid sublimation of the produced secondary

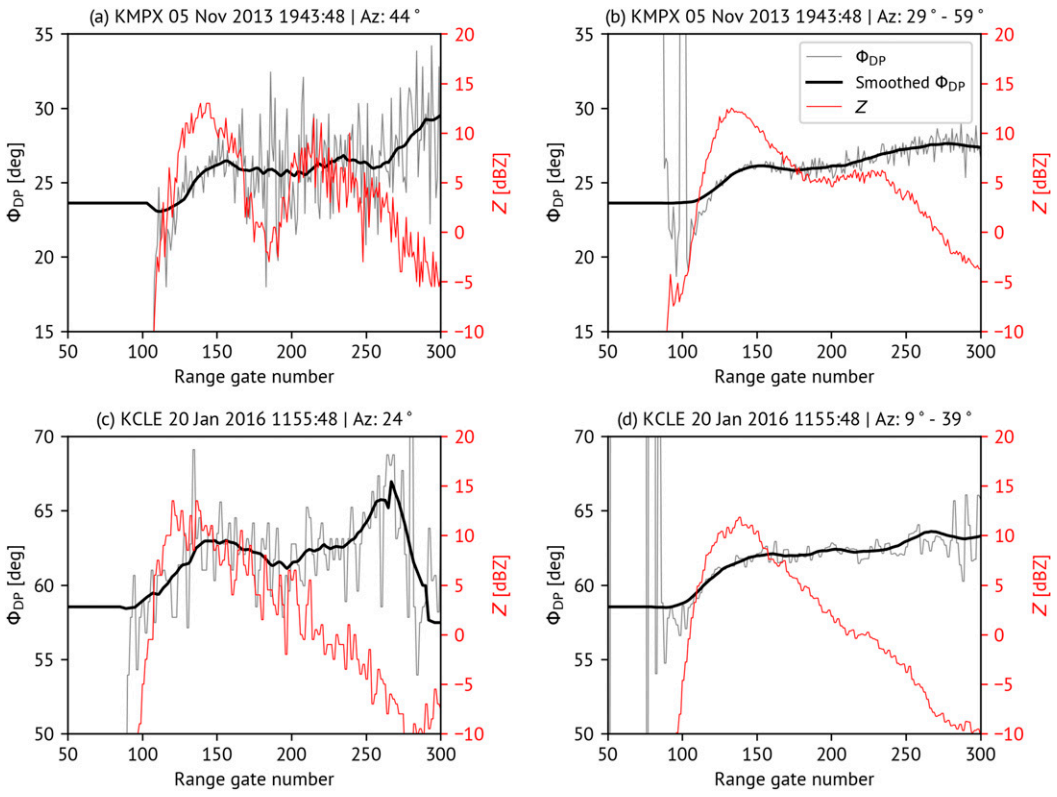

FIG. 5. Example Φ_{DP} (gray) and Z (red) range profiles from the 4.5° elevation scan for (a),(c) a single azimuth and (b),(d) a 30° sector average centered on the single azimuth for selected cases and times. Range gates 50, 100, 150, 200, 250, and 300 correspond to AGL heights of approximately 0.99, 2.00, 3.02, 4.06, 5.13, and 6.21 km, respectively.

ice (Korolev et al. 2020). However, compelling observational evidence of SIP due to sublimation exists (Oraltay and Hallett 1989; Dong et al. 1994; Bacon et al. 1998), although has been limited so far to laboratory studies of individual crystals. These studies determined that dendrites and irregularly shaped crystals are prone to fracturing during sublimation while plates and columns are not, and that SIP was more likely in drier environments and for larger particles.

Nine of the 12 cases exhibit this signature, all of which occur within the sharp vertical gradient of RH_i (Fig. 4) and peak in the top half of the Z gradient. It is not immediately clear why three cases lack this signature (Figs. 4e,g,h). In general, these cases featured less-pronounced K_{dp} signatures aloft and, in two of the cases, very weak Z (Figs. 1e,h), although other cases with such low Z values still produced the signature (Figs. 1d,k). A cursory analysis was performed to determine the expected dominant crystal habit based on the RAP temperature and ice supersaturation fields (Bailey and Hallett 2009). Of the three cases that did not exhibit a K_{dp} enhancement in the sublimation layer (Figs. 4e,g,h), the DGL was only either weakly or subsaturated, with the dominant crystal habit expected to be plates. In contrast, many of the cases that did exhibit prominent K_{dp} enhancements did exhibit large supersaturations within the DGL (e.g., Figs. 4a,c,d), suggesting dendritic crystals could have been dominant and prone to SIP. That said, a number of cases that did exhibit K_{dp} enhancements were only weakly saturated within the DGL (e.g., Figs. 4i,k,l), although the onset of the signature did appear to be correspond with increasing saturation within the DGL in some instances (e.g., Fig. 4l). While this analysis is subject to errors in the RAP moisture fields and it is difficult to rule out the influence of more-irregular crystal habits, this serves as at least circumstantial evidence of the role crystal habit may be playing in the potential SIP. Beyond the dominant crystal habit, it stands to reason that if the RH_i gradient is too weak, snowflakes may completely sublimate before reaching sufficiently dry air for appreciable SIP. Similarly, if particle concentrations are too low, observable SIP may not occur.

The average median sublimation-layer depth is 916 m, with a maximum median depth of 1116 m (Fig. 3d), although a large degree of within-case variability exists in part as a result of occasional jumps in the heights of the detected sublimation-layer top. This is comparable to but somewhat larger than seen in Forbes and Hogan (2006), who found an average layer depth of 630 m with 90% of cases having depths less than 1000 m. However, they defined their sublimation layer differently, and both beam broadening and azimuthal averaging of heterogeneous sublimation-layer depths will act to deepen the RDQVP-derived depths. There is no obvious relation between the sublimation-layer depth and the bulk changes of any of the polarimetric radar variables, except for perhaps a weak positive relation between ΔZ and sublimation-layer depth (Figs. 3a,d).

3. 1D spectral bin model simulations

a. Model description

The aforementioned RDQVPs were used to initialize a 1D semi-Lagrangian spectral bin model of snow (Carlin and Ryzhkov 2019). This model treats sublimation/deposition, melting, and evaporation/condensation of particles. Here, particles are assumed to be unrimed aggregates and are treated as homogeneous oblate spheroids with bulk densities following Brandes et al. (2007). Particle concentrations in each size bin are found assuming number flux conservation within each bin, with interactions and transfers between bins (including breakup/SIP) excluded. The rate of sublimation of a given particle with diameter D is calculated according to Pruppacher and Klett (1997),

$$\frac{dm_i(D)}{dt} = 4\pi c S_i G_i, \tag{2}$$

where m_i is the mass of ice and c is the capacitance (McDonald 1963; Mitra et al. 1990) of a given particle; S_i is the supersaturation with respect to ice; and G_i is the thermodynamic and vapor diffusivity factor equal to

$$G_i = \left\{ \left(\frac{L_s}{k f_h T} \right) \left[\left(\frac{L_s M_w}{RT} \right) - 1 \right] + \left(\frac{RT}{f_v D_v M_w e_{s,i}} \right) \right\}^{-1}, \tag{3}$$

where L_s is the enthalpy of sublimation; k is the thermal conductivity of air; f_v and f_h are the vapor and thermal ventilation coefficients, respectively (Hall and Pruppacher 1976); T is the ambient air temperature; M_w is the molecular weight of water; R is the universal gas constant; D_v is the diffusivity of water vapor; T is the ambient temperature; and $e_{s,i}$ is the saturation vapor pressure with respect to ice at ambient temperature T. Equation (2) has been shown to accurately represent the sublimation process when compared with in situ observations (Nelson 1998; Field et al. 2008). Temperature and moisture feedbacks with the environment are included in the model, but vertical air motion, horizontal and vertical advection, and turbulent mixing are excluded.

The model output can be coupled to a polarimetric radar operator (Ryzhkov et al. 2011), which assumes an aspect ratio for aggregates of 0.6 (e.g., Korolev and Isaac 2003; Hogan et al. 2012; Garrett et al. 2015), a canting angle width distribution of 40° (Hendry et al. 1987), and calculates the effective relative permittivity of dry snowflakes using a Maxwell Garnett (Maxwell Garnett 1904) mixing formula for a topology of an air matrix with ice inclusions.

b. Model initialization

The model environment was initialized using the RAP analysis column nearest the radar site once the RDQVP Z consistently exceeded 0 dBZ somewhere in the column. The model depth was 5 km, with the RAP data linearly interpolated to a 10-m vertical grid spacing. After initialization, the environment evolved in response to only the microphysical processes within the 1D model. New simulations were also initiated hourly using each RAP analysis up until the hour that contained the mean snowfall start time of all available observations. Each simulation was run until the snowfall rate at the lowest model level reached 0.1 mm h^{-1}, at which point snow was considered to have reached the surface.

The snow particle size distributions (PSDs) at the top of the model were initialized from the RDQVPs. First, an ad hoc attempt to correct for Z_{DR} bias was made by adjusting Z_{DR} so that values in regions believed to be dominated by dry aggregates (i.e., large Z near the surface) were near 0.1–0.15 dB, following Bukovčić et al. (2020). Next, the mean-volume diameter D_m and IWC were retrieved using two recently proposed sets of polarimetric relations. The first set proposed by Ryzhkov and Zrnić (2019) uses Z_{dr} and K_{dp} to retrieve D_m and IWC:

$$D_m(Z_{dr}, K_{dp}) = -0.1 + 2.0 \left(\frac{Z_{dp}}{K_{dp}\lambda} \right)^{1/2} \quad \text{and} \tag{4a}$$

$$\text{IWC}(Z_{dr}, K_{dp}) = 4.0 \times 10^{-3} \frac{K_{dp}\lambda}{1 - Z_{dr}^{-1}}, \tag{4b}$$

where $Z_{dp} = Z(1 - Z_{dr}^{-1})$ and the lowercase subscripts indicate linear units of mm^6 m^{-3}. This set of equations benefits from being relatively immune to variations of snowflake shape and orientation but is sensitive to density variations (i.e., degree of riming) and is prone to errors due to Z_{DR} bias, particularly at the low values typical of aggregated snowflakes. A second set, described in Bukovčić et al. (2018, 2020), uses Z and K_{dp}:

$$D_m = 0.67 \left(\frac{Z}{K_{dp}\lambda} \right)^{1/3} \quad \text{and} \tag{5a}$$

$$\text{IWC}(Z, K_{dp}) = 3.3 \times 10^{-2} (K_{dp}\lambda)^{0.67} Z^{0.33}. \tag{5b}$$

In contrast with Eq. (4), this set of relations has the advantage of being immune to Z_{DR} miscalibration and exponents that are practically invariant with respect to particle characteristics; however, both Eqs. (5a) and (5b) are sensitive to particle aspect ratios and orientations, with Eq. (5b) additionally sensitive to particle density. Owing to these complementary strengths and considering each set's optimal ranges, we combined these relations into a third set that serves as the primary set for this study, with D_m retrieved using Eq. (5a) and IWC retrieved using Eq. (4b) for $Z_{DR} \geq 0.4$ dB and Eq. (5b) for $Z_{DR} < 0.4$ dB. In Eqs. (4) and (5), both Z and Z_{dp} are in linear units of mm^6 m^{-3}, K_{dp} is in degrees per kilometer, λ is the radar wavelength in millimeters (assumed to be 103.7 mm, within the WSR-88D's operating range), D_m is in millimeters, and IWC is in grams per meter cubed. Note that while technically both Z and Z_{DR} are needed to compute Z_{dp}, here we use IWC(Z, Z_{dr}, K_{dp}) to refer to the combined set of equations while IWC(Z_{dr}, K_{dp}) refers to Eq. (4b). PSDs are assumed to follow a gamma distribution,

$$N(D) = N_0 D^{\mu} e^{-\Lambda D} dD, \tag{6}$$

where $\mu = 0$ (i.e., an inverse-exponential distribution). Combined with the assumption of an inverse relationship between particle size and density (e.g., Brandes et al. 2007), the total number concentration N_t (m^{-3}) can be found according to

$$\log_{10}(N_t) = 6.69 + 2\log_{10}(\mathrm{IWC}) - 0.1Z \quad (\mathrm{dB}Z), \tag{7}$$

and the slope parameter (Λ; mm^{-1}) and intercept parameter (N_0; $\mathrm{m}^{-3}\,\mathrm{mm}^{-1}$) are subsequently found according to (e.g., Ulbrich 1983)

$$\Lambda = 4/D_m \quad \text{and} \tag{8}$$

$$N_0 = \Lambda N_t. \tag{9}$$

The model time step was 60 s, with PSDs updated every time step using the RDQVP observation closest in time. Because of the model's fixed height grid, the PSD was chosen from the highest observed Z in the column (up to the model top) as a proxy for the snow PSD prior to the start of sublimational losses.

c. Verification metrics

Defining precisely when snow first reached the surface at a given location proved somewhat difficult. As such, a variety of observation sources were compiled and used, each with their own advantages and disadvantages. The first was the RDQVP data from Fig. 1, where a Z value of 0 dBZ at the lowest usable height (typically 20.0 m above radar level) was chosen to denote the snow start time. This threshold is arbitrary, and the temporal resolution of the data is only 5–10 min, but the RDQVP data have the advantage of being collocated in space with the simulation location. In addition, depending on the precipitation coverage and lowest level of usable data, the azimuthally averaged RDQVP may be unrepresentative of the snow start time at a given location. Automated Surface Observing System (ASOS; ASOS Program Office Staff 1998) observations were also used and have the advantage of being at or very near the simulation location for most cases and have a native temporal resolution of 1 min. However, it is possible for ASOS to err when determining precipitation type at the onset of light precipitation and miss extremely gradual onsets of snow due to rising "adaptive baselines" (ASOS Program Office Staff 1998). When available, multiple nearby ASOS sites from the surrounding area were included to get a more comprehensive sense of the observed start time. Reports from the Meteorological Phenomena Identification near the Ground (mPING; Elmore et al. 2014) project were included. These reports have the potential advantage of high spatial resolution and the ability to report as soon as precipitation is observed but are also subject to human error and biases due to time of day and radar location relative to population/observer density. While there is no guarantee that snow will be reported at its start, it stands to reason that the initial onset of precipitation would be deemed worthy of reporting by many observers. Because the number and density of available mPING reports varied appreciably among events, we subjectively identified the most representative first few snow reports by their proximity to the simulation location that were succeeded by additional snow reports. While the range of distances and reporting frequencies make no one observation source a perfect metric for determining snow start time, we believe that together they provide a holistic picture that is sufficient for evaluating the simulation results.

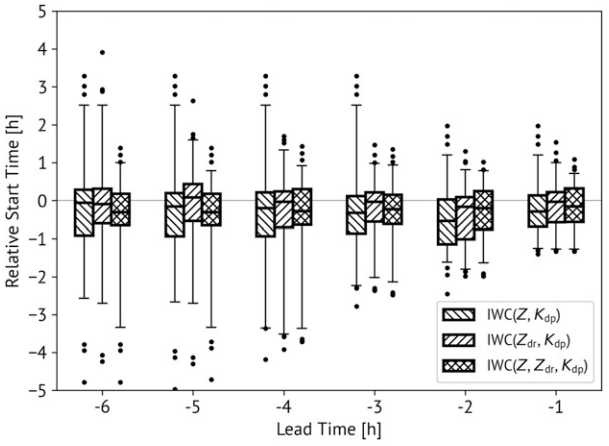

FIG. 6. Boxplots of model-predicted snowfall start times relative to all observations using IWC(Z, K_{dp}) [Eq. (5)], IWC(Z_{dr}, K_{dp}) [Eq. (4)], and IWC(Z, Z_{DR}, K_{dp}) as a function of lead time, where a negative relative start time indicates that the model start time preceded the observed start time. Boxes depict the 25th–75th percentiles, and whiskers depict the 5th–95th percentiles.

A representative time that defines the 0-h relative start time was determined using the mean start time of all available observation sources for each case. Because the model runs were initialized from on-the-hour RAP analyses but the mean observed start time could occur at any time, the model lead time was calculated with respect to the start of the hour containing the mean start time (e.g., for a mean observed start time of 1845 UTC, a lead time of 0 h on the abscissa corresponds to 1800 UTC). In this way, the defined lead times are conservative, with a lead time of 1 h actually corresponding to mean observed start times anywhere from 60 to up to 120 min later. The maximum lead time available for each case depends upon when appreciable Z first appeared.

d. Results

Figures 6 and 7 compare the model-predicted start times of surface snowfall with the aforementioned observation sources. Overall, the simulations do a good job of capturing the observed start time of surface snowfall (Fig. 6). As far out as 6 h, the median bias in projected snowfall start time for the combined set of equations is only −18.5 min. This slight early bias persists at all lead times, decreasing to −9.5 min at a lead time of 1 h. The interquartile range is also reasonably narrow, spanning 50 min at 6 h out and 53 min at 1 h out. As expected, the full scope of the distributions narrows in time because there is less dry air to erode and, in theory, the RAP analyses used as the model background contain fewer errors. There is some evidence that using the combination of retrieval equations [i.e., IWC(Z, Z_{dr}, K_{dp})] results in more constrained forecasts, with narrower interquartile ranges at all except the smallest lead times and less-extreme outlying values, especially when compared with using IWC(Z, K_{dp}) alone. For example, the MAD of the model-predicted start times using IWC(Z, Z_{dr}, K_{dp}) are 15.0, 9.0, and 5.5 min smaller than when using IWC(Z, K_{dp}) for 6-, 4-, and 2-h lead times, respectively. Similarly, for the same

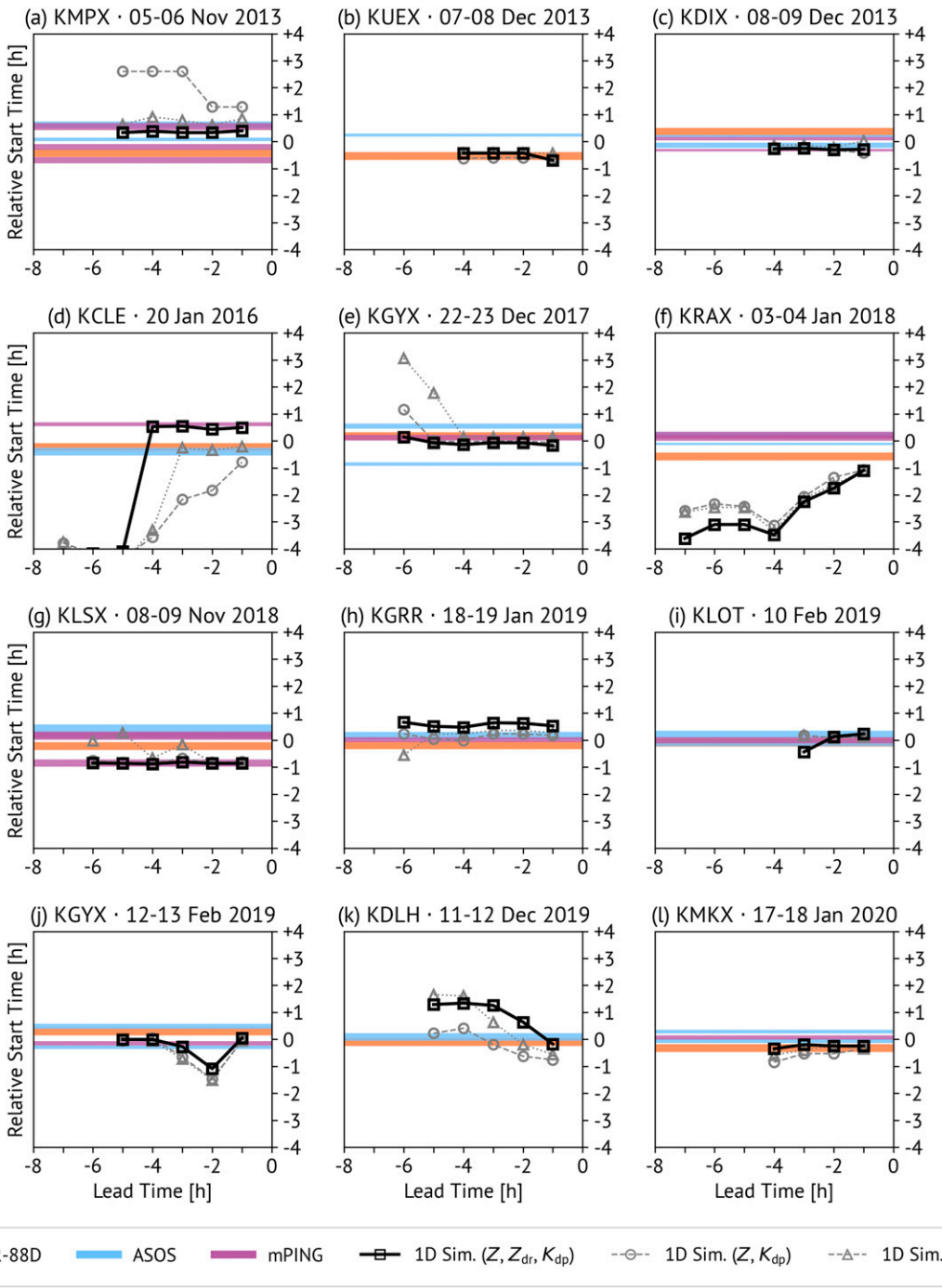

FIG. 7. Model-predicted snowfall start times as a function of lead time relative to observed snowfall start times for the WSR-88D estimates (orange), ASOS stations (blue), and mPING reports (purple) for each of the 12 cases using each set of retrieval equations [Eqs. (4) and (5)] and their combination. The width of the observation lines is inversely proportional to their distance from the radar site.

experiments and lead times the number of relative start times more than 1-h from the observed start times are reduced by 10.4%, 10.4%, and 14.6%, respectively. Because all observation sources are used to compute the relative start times, there will inherently be some spread even for a forecast that exactly matches the mean observed start time. Interquartile ranges computed only with respect to the mean start time for each case rather than all observation sources decrease from 44 min at a 6-h lead time to 39 min at a 1-h lead time, with similar median start time biases (not shown).

The predicted snowfall start times as a function of lead time are shown separately for each case in Fig. 7. It is clear that the aforementioned variability in observed start times for a given case is indeed present, with some cases (e.g., Figs. 7a,b,e,g) spanning a nearly 2-h window around the mean that highlights the inherent uncertainty of identifying a precise snowfall start time for a point location. Many of the cases exhibit remarkable consistency in their predicted start times across lead times (e.g., Figs. 7a,c,e,g,l). Some cases, however, exhibit decreases in bias as the lead time decreases, which is likely responsible for the narrowing of the distributions in time in Fig. 6. These shifts in predicted start time often occur gradually (e.g., Figs. 7f,i,k). This could be indicative of errors in the model background decreasing with time, but more likely represents either a consistent bias in the retrieved snow parameters (i.e., predicting snowfall start times that are some constant duration after model initialization, which naturally get closer to the observed start time as the lead time decreases) or, more specifically in the case of a decreasing early bias (e.g., Figs. 7f,i), a diminishing influence of contaminated retrievals early in the period associated with suspected SIP (discussed further in section 4). In contrast, the KCLE 20 January 2016 case (Fig. 7d) exhibits a sudden shift of many hours at a 4-h lead time, which could indicate errors in the model background undergoing a correction.

e. Case study: 8 December 2013 snowstorm

To demonstrate the model's performance for a high-impact weather event that proved challenging to forecast, the 8 December 2013 case at KDIX (Fig. 1c) is examined in more detail. On this date, unexpectedly heavy snow fell along the Maryland–Pennsylvania border and into south-central New Jersey, with cold-air damming present on the leeward side of the Appalachian Mountains. This particular event garnered national attention because the onset of the most intense snowfall coincided with the beginning of a highly publicized National Football League game in Philadelphia, Pennsylvania. Game announcers repeatedly informed the audience that local forecasters had only predicted about 2–3 in. (5.1–7.6 cm) of snow to fall after 2000 UTC. By halftime (about 1930 UTC), over 8 in. (20 cm) of snow had accumulated on the field and visibilities had dropped to below 0.4 km (0.25 mi). More than 2500 flights were canceled, with delays exceeding 4.5 h at Philadelphia International Airport, and a 50-car pileup and numerous other accidents occurred in the greater Philadelphia area with one fatality reported (Associated Press 2013; Mohney G 2013; National Centers for Environmental Information 2014). By the time the snow stopped falling at about 0000 UTC 9 December 2013, some locations reported more than 30 cm (12 in.) of snow. In the lead-up to this event, forecasters at the NWS noted the significantly dry air that would have to be overcome before snow could reach the surface and described uncertainty about the rate at which this would occur as a primary forecast challenge.

Figure 8a shows the 1200 UTC 8 December 2013 RAP analysis sounding at the gridpoint nearest McGuire Field in Wrightstown, New Jersey (KWRI), the ASOS site nearest the KDIX radar with human-augmented METARs. The entire profile is below 0°C and supportive of snow, with a deep, nearly saturated layer above 600 hPa (≈4.3 km AGL) and the layer from −12° to −18°C that is favorable for planar and dendritic growth being located between roughly 4.6 and 5.7 km AGL. However, a substantial layer of extremely dry air was present beneath this layer, with dewpoint depressions exceeding 40°C and relative humidity with respect to liquid water as low as 2%. Light snow was first observed at KWRI at 1616 UTC (Fig. 8d) as visibilities dropped below 16 km. However, by 1807 UTC, heavy snow was reported and lasted until about 1913 UTC, with attendant drops in visibility below 0.4 km. Visibility rates increased over the next hour so that only light snow was observed after 1943 UTC. Consistent light ($<5\,\mathrm{m\,s^{-1}}$) northeasterly winds, an abrupt increase in the 2-m dewpoint at the onset of heavy precipitation, and a more modest decrease in temperature are all consistent with sublimation, rather than a front, being the primary driver of changes in the environment.

The simulation was initiated at 1200 UTC (i.e., with a 4-h lead time), with the time series of retrieved N_0 and Λ from the combined retrieval equation set that were used to initialize the model shown in Figs. 9a,b. The PSDs start out being steep, with Λ values of 4–6 $\mathrm{mm^{-1}}$ and $N_0 > 10^5\,\mathrm{m^{-3}\,mm^{-1}}$. Both of these parameters gradually decrease over the period as dry air is eroded and the saturated layer extends toward the ground, the precipitation layer becomes deeper, and aggregation becomes more dominant, with $\Lambda \approx 1.0\,\mathrm{mm^{-1}}$ near the end of the period characteristic of heavily aggregated snow (e.g., Lo and Passarelli 1982). This type of evolution was typical and observed in nearly all the cases examined. Figures 9c,d compares the observed and simulated Z. In general, there is fairly good correspondence between the two, with a Z "front" steadily descending as sublimation erodes the dry layer and realistic values of simulated Z. There is a slight divergence between the observations and simulated results after 1600 UTC as the simulated Z rapidly descends to the surface as precipitation rates aloft increase while the observations indicate a steady rate of descent that reaches the surface (using a 0-dBZ threshold) at 1646 UTC. One suspected reason for this is how PSDs are determined at each model level: by assuming flux conservation, changes in the PSD aloft are instantly reflected throughout the column, while in reality there is an appreciable delay between when snow is generated aloft and when these changes reach the surface (e.g., the slanted fallstreaks visible in Fig. 1c). This may partially explain the slight but consistent median early bias discussed in section 3d. In addition, the azimuthal averaging involved in generating the RDQVP obfuscates the gradient in snow from west-southwest to east-northeast apparent in the plan position indicator scans. The cooling and moistening due to sublimation takes place within a narrow ≈500-m-deep layer (Figs. 9e,f), in good agreement with Forbes and Hogan (2006); the instantaneous cooling rate reaches maxima of −18.3 and $-16.8\,\mathrm{K\,h^{-1}}$ at 1256 and 1451 UTC, respectively. These values are associated with observed Z values of only 16.5 and 18.9 dBZ, respectively, highlighting the lack of reliable correspondence between Z and sublimational cooling due to the sensitivity of Z to the largest snowflakes.

Figure 10 compares the simulated surface snowfall rate with the KWRI ASOS observations. Because our model calculates

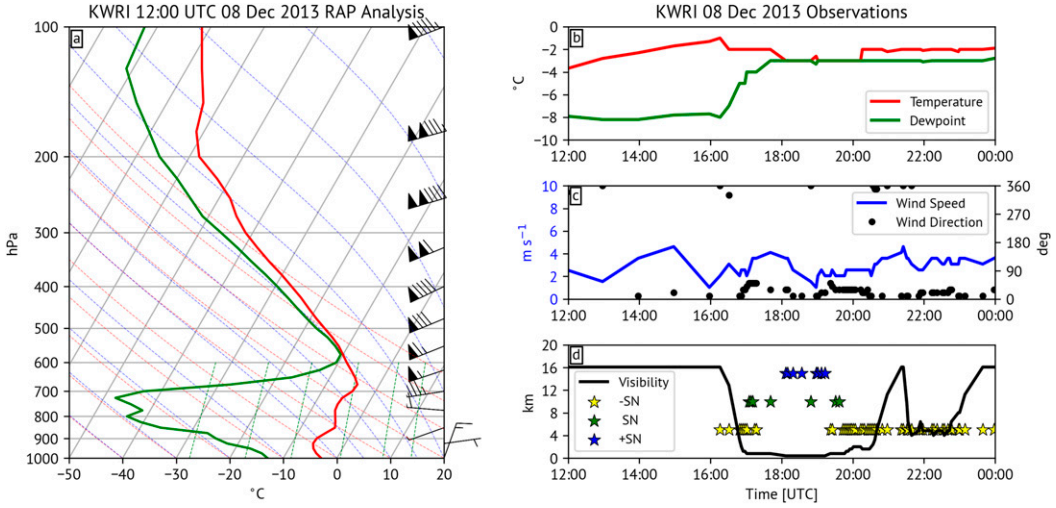

FIG. 8. (a) Skew T–log$p$ from the 1200 UTC 8 Dec 2013 RAP analysis from the grid point nearest KWRI (40.015°N, −74.592°E), and observed (b) temperature (red; °C) and dewpoint (green; °C), (c) wind speed (blue; m s^{-1}) and wind direction (black; °), and (d) visibility (km) and present weather condition (where yellow = light snow, green = moderate snow, and blue = heavy snow) at the KWRI ASOS.

the (liquid equivalent) snowfall rate while the ASOS only reports light (−SN), moderate (SN), and heavy (+SN) snow as a function of visibility (National Weather Service 1996), we converted the simulated snowfall rate to equivalent snowfall intensity categories using the Society of Automotive Engineers (SAE) Ground De-icing Committee definitions (Leroux 2019) following Rasmussen et al. (1999) [light snow −SN $<$ 1 mm h^{-1}, 1 $\leq$ snow (S) $<$ 2.5 mm h^{-1}, and heavy snow (+SN) $\geq$ 2.5 mm h^{-1}]; the consistency of these relations was confirmed by calculating the extinction coefficient (used to estimate visibility; Bukovčić et al. 2021) explicitly from the 1D model. Overall, there is fair agreement between the model and the KWRI observations. The model does well at predicting the start time of snow at KWRI, with a simulated start time of 1607 UTC versus the 1616 UTC observed. At the time snow is first reported, the observed RH$_i$ at KWRI is only 59% while in the simulation it is 49%. The simulated snowfall rate does increase more rapidly than observed, reaching a heavy snowfall rate by 1634 UTC. Simulations performed using the two other sets of retrieval equations [Eqs. (4) and (5)] showed slightly slower increases in intensity, beginning at 1625 and 1638 UTC and reaching heavy snowfall rates by 1703 and 1714 UTC, respectively. While KWRI did not report heavy snow until 1807 UTC, other sites in the area reported a much more rapid onset of heavy snow, such as Philadelphia International Airport (KPHL) by 1642 UTC and South Jersey Regional Airport (KVAY) by 1702 UTC. Thus, considering KWRI is 17 km to the east-northeast of KDIX and other sites reported heavier snow much sooner, these results lend credence to the ability of the model to realistically simulate the overcoming of this low-level dry air through sublimation.

Given the good agreement between the 1D simulation and what transpired for this event, it is instructive to contextualize the 1D model performance with other available nowcasting tools. The RAP/HRRR is a primary (although by no means only) tool for nowcasting and short-term forecasting available to forecasters. Unfortunately, a comparison between the simulated and retrieved PSDs could not be performed because the archived RAP files do not include hydrometeor variables. However, more indirect metrics can be used to ascertain how well the RAP simulated this event relative to the 1D simulation.

Figure 11 shows the evolution of the RH$_i$ profiles from the 1200 UTC 8 December 2013 RAP forecast and the 1D simulation initialized from the model analysis. Both models exhibit a gradual descent of the saturated layer, but the RAP forecast exhibits more rapid moistening and a deeper sublimation layer, with the bottom of the saturated layer extending nearly 1 km lower than the 1D simulation by 1400 UTC (Fig. 11c). Within the narrow sublimation zone, moistening can occur extremely rapidly. For example, the RH$_i$ at 2.0 km AGL increases from 10% to 90% in just 29 min from 1444 to 1513 UTC in the 1D simulation.

However, after 1400 UTC the solutions diverge significantly. The 1D simulation continues to saturate downward at an increasing rate due to the enhanced precipitation flux at this time (Fig. 1c), with the saturated layer descending from ≈1.7 km AGL to near the surface between 1600 and 1700 UTC and snow reaching the surface early in this period. In contrast, the RAP's descent of the nearly saturated layer essentially ceases at 1500 UTC, with no further moistening at low levels. Concurrent with this cessation of moistening is the appearance of much drier air aloft, with RH$_i$ at 1600 UTC decreasing to as low as 46% at 3.3 km. Such dry air aloft prevents snow from penetrating down to lower levels to continue saturating the dry air, if not preventing the formation of heavier precipitation altogether. This dry air aloft is itself eventually moistened and begins to erode by 1700 UTC, but by this point heavy snow was already being observed in the region and the low levels are still substantially subsaturated. We believe this intrusion of dry air aloft to be erroneous as there is no suggestion of precipitation

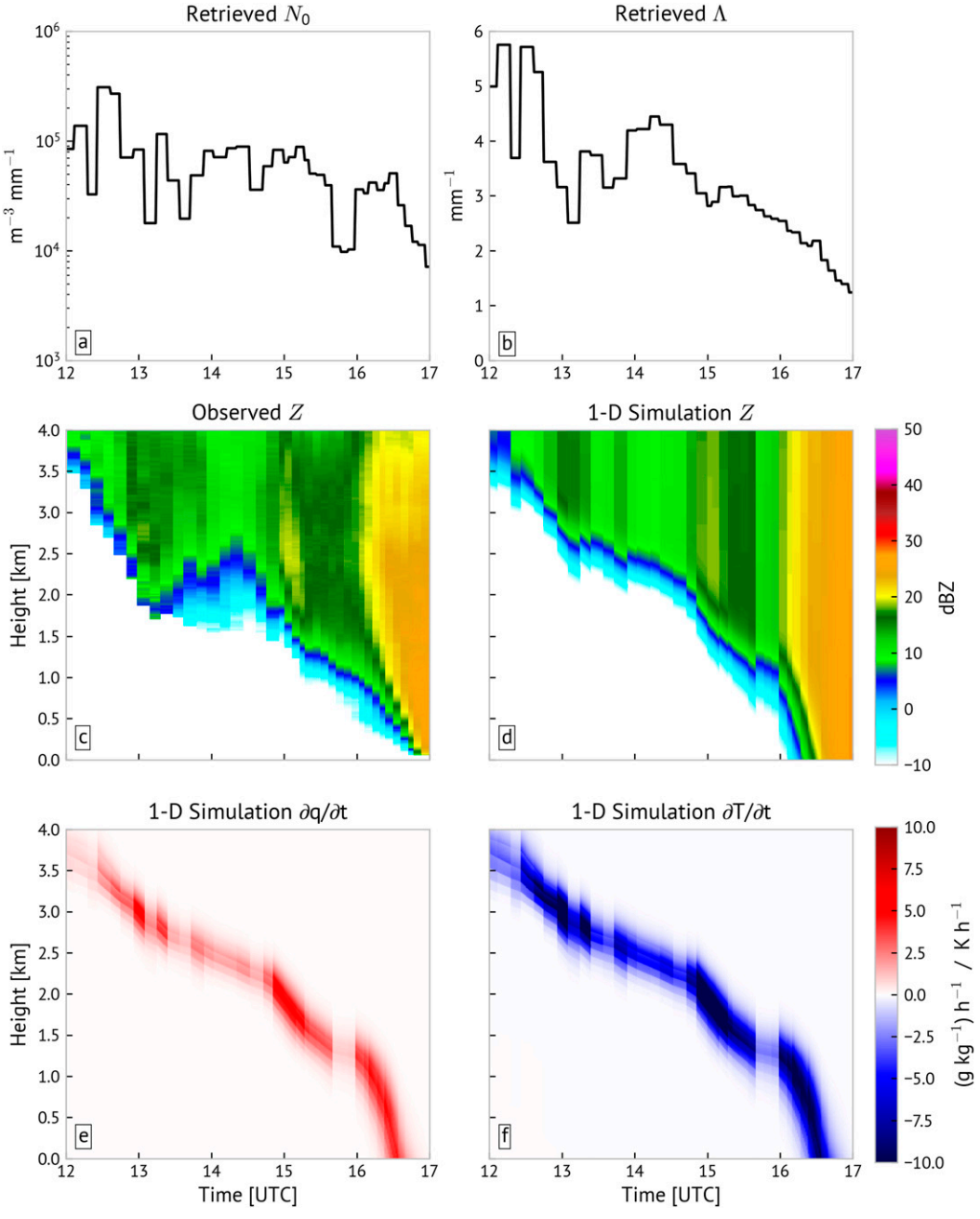

FIG. 9. Time series of the (a) N_0 and (b) Λ retrieved from the KDIX RDQVP that were used to initialize the 1D model, and a comparison of (c) the observed Z from the KDIX RDQVP and the (d) Z, (e) moistening rate [(g kg^{-1}) h^{-1}], and (f) heating rate (K h^{-1}) from the 1D model simulation between 1200 and 1700 UTC.

erosion or sublimation aloft (e.g., as seen in Figs. 3 and 7 of Griffin et al. 2018). An examination of the source of this dry air revealed that it first appeared during the 1200 UTC analysis over West Virginia and advected over the area. While a full forensic examination of the source of this dry air is beyond the scope of this study, a cursory examination revealed anomalously large observation analysis increments between the 1200 UTC RAP analysis and the 1100 UTC 1-h forecast, suggesting an issue during the data assimilation routine resulting in a poor analysis field. Suffice it to say that, whatever the reason for this erroneous dry air, this error appears to have had significant downstream consequences and demonstrates the usefulness of spatially averaged radar data, such as quasi-vertical profiles (QVPs), and 1D models for nowcasting and determining when model forecasts may have gone awry.

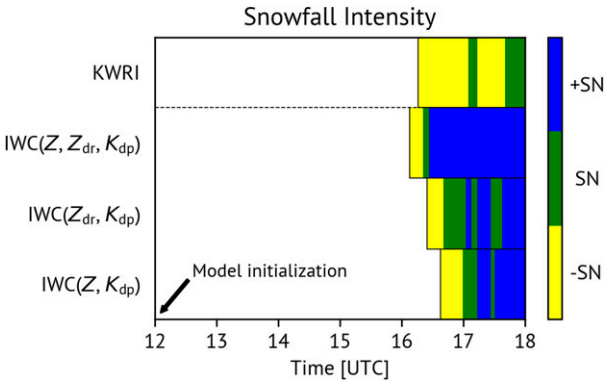

FIG. 10. Evolution of the observed snowfall rate at KWRI and the simulated snowfall rate from the 1D model using each of the three sets of retrieval equations. The snowfall intensity colors correspond to those in Fig. 8d.

4. Discussion of sensitivities and future work

Despite the encouraging results shown herein, there are a number of important caveats. One is the simplified nature of the 1D model. While it was demonstrated that such a model can generally simulate the evolution of the environment with sufficient accuracy and has the benefit of being computationally inexpensive, the exclusion of dynamic coupling to simulate a response in the vertical velocity field to the cooling rate, and the attendant adiabatic temperature changes, remains a shortcoming. Similarly, horizontal advection of temperature and moisture is neglected. This can be an important factor if the dry air is being replenished, and while we tried to select cases where this was minimized, it may be responsible for some of the more pronounced poor performances in the cases examined (e.g., 3–4 January 2018 at KRAX) or the overall slight early bias observed. Going forward, it would be straightforward to implement an advection parameterization using environmental time tendencies, should such profiles be known.

The polarimetric snow PSD retrievals represent another source of uncertainty and possible error. Some model parameters, such as the maximum particle dimension at which to truncate the PSD, had almost no effect on the results as the large majority of ice mass is concentrated at smaller particle sizes. Other properties, such as snowflake orientation, shapes, and density, are difficult to know a priori. When considering the full range of both mean particle aspect ratio and canting angle distribution widths, the prefactor of Eq. (5b) may vary by up to a factor of 3.8 (Bukovčić et al. 2018). Some of the cases chosen may not have been well-characterized as aggregates (e.g., KDLH on 11–12 December 2019, which exhibited mean Z_{DR} values near 1.0 dB; Fig. 2) and thus may have been better simulated using a modified PSD retrieval equations. As polarimetric IWC and snow PSD retrieval methods continue to be refined or other multiparameter retrieval methods are developed, improvements in reliability and accuracy should ultimately transfer to applications such as this.

The radar data quality matters. One outstanding uncertainty relates to potential Z_{DR} biases. We attempted to correct for these, and the combined set of retrieval equations was used to minimize the impacts of these biases. The exact adjustments needed were unknown, however, and the need for an adjustment were known more confidently for suspected negative biases versus positive biases. We performed a number of sensitivity experiments where we shifted the Z_{DR} adjustment by ± 0.1 dB, the desired Z_{DR} calibration accuracy of the WSR-88D network (Ryzhkov et al. 2005). Shifting the corrected Z_{DR} field by $+0.1$ dB delayed the mean snowfall start time by 13 min, while shifting it by -0.1 dB caused the mean snowfall start time to be 23 min earlier. In a few instances, the adjusted Z_{DR} resulted in a drastic shift in start time as the snowfall rate fell just short or narrowly surpassed 0.1 mm h^{-1}, highlighting the impact of relying on fixed thresholds. The azimuthal averaging necessary to obtain sufficiently accurate estimates of K_{dp} also necessarily smooths out heterogeneities in the precipitation field. In reality, snowflakes may travel fairly large horizontal distances from their source region before reaching the ground. Future work could explore the potential for backward snowflake trajectories to define a more Lagrangian quasi-vertical profile. Other radar data spatial averaging techniques optimized for locations farther from the radar, such as columnar vertical profiles (CVPs; Murphy et al. 2020) and range- and azimuth-defined QVPs (raQVPs; Kumjian et al. 2020), could also be used to initialize models and better characterize the local precipitation profile.

The potential evidence of sublimational SIP also deserves further investigation. At first glance, sublimational SIP may seem inconsequential because it both conserves mass (thereby not affecting the total heat extracted from the environment during the sublimation process) and is a self-limiting process as the dry air responsible for the SIP rapidly sublimates the resultant fragments (Korolev et al. 2020). The generally good performance of the 1D simulations sans SIP would seem to bolster the argument of sublimational SIP being fairly inconsequential. However, despite conserving mass, the production of fragments with much slower terminal velocities can modify the vertical distribution of sublimational cooling, which could have nonlinear effects on subsequent distributions of cooling and moistening. More straightforwardly, caution must be exercised in using PSD retrievals in such regions, as appreciable SIP likely results in decidedly nonexponential PSDs that violate the underlying assumption used to derive the PSD parameters (i.e., $\mu = 0$), and at the very least exacerbates issues with regard to the efficacy of the retrieval methods in regions with multiple disparate particle types. For the most part, the heights the PSDs were chosen from to initialize the model remained just above the layer of enhanced IWC/K_{dp}, although it is difficult to totally exclude the possibility of minor impacts. As a sensitivity test, we initialized a second set of simulations instead using the PSD at the maximum IWC (rather than Z). The impacts of doing so were relatively modest, with the mean start time of surface snowfall shifted 21 min earlier and the median start time shifted 13 min earlier. However, in one case (11–12 December 2019 at KDLH) the start time became over 3 h earlier and in a few instances (e.g., 7–8 December 2013 at KUEX) the start times were actually delayed, further demonstrating the nonlinear effects of changing the PSD. Also,

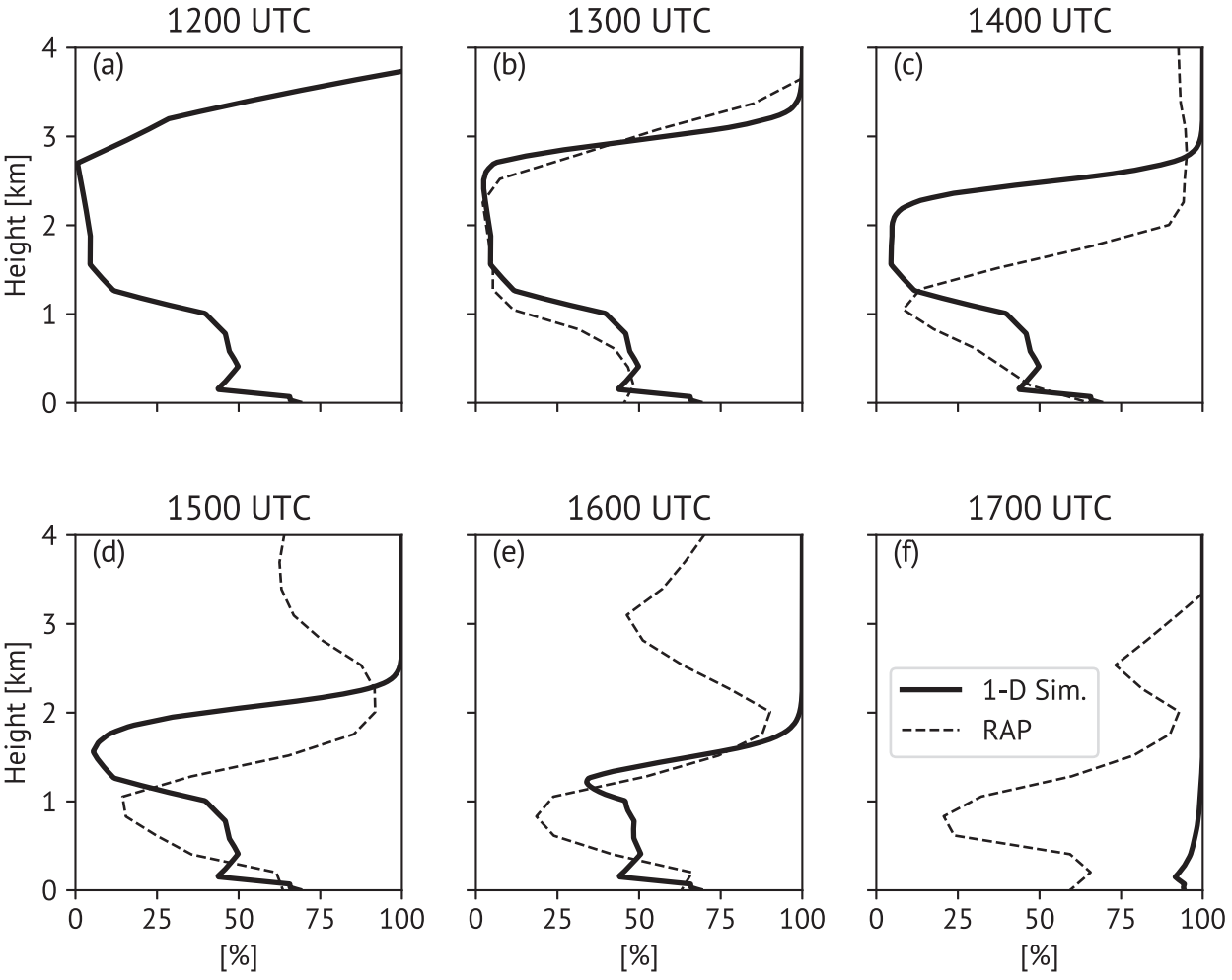

FIG. 11. Evolution of the vertical profile of relative humidity (with respect to ice) from the 1D simulation (solid) and the RAP forecast initialized at 1200 UTC 8 Dec 2013 (dashed).

while there is convincing observational evidence of the existence of sublimational SIP as discussed in section 2b, little is known about sublimational SIP from aggregates or the resulting fragment characteristics (e.g., number, shape, size), all of which would affect their subsequent lifetime. In addition to examining more cases, a more thorough investigation of the plausibility of sublimational SIP using numerical simulations and electromagnetic scattering calculations is planned for a follow-up study.

5. Summary and conclusions

Sublimating snow presents a forecasting and nowcasting challenge for predicting when snowfall may reach the surface through antecedent dry air masses and can have dynamical consequences (e.g., turbulence generation, frontogenesis), yet it remains comparatively less studied than other microphysical processes. This study sought to exploit dual-polarization radar observations of sublimating snow to both gain insight into the microphysical processes at play and, in conjunction with a 1D bin model, nowcast the start time of snow reaching the surface through dry air.

Through analyzing RDQVPs of 12 cases of sublimating snow, it was revealed that there is generally a pronounced decrease in Z, marginal decrease in Z_{DR}, and relatively constant ρ_{hv} through the sublimation layer. These Z_{DR} observations are consistent with the effects of particles becoming more randomly oriented due to turbulence and/or exhibiting decreasing anisotropy, although disentangling the potential causes of such trends in Z_{DR} proved difficult. In addition, a majority of cases exhibited a pronounced increase in K_{dp} in the sublimation layer coincident with the Z and RH_i gradients that is believed to be novel polarimetric evidence of secondary ice production due to sublimation.

A 1D bin microphysical model initialized using RAP profiles and time-varying snow PSDs retrieved from the RDQVPs displayed skill in predicting the start time of snow at the surface at lead times of up to 6 h, with a median early bias of −18.5 min that decreased to just −9.5 min at a 1-h lead time and with 50% of simulations falling within a 50-min window relative to the observed start time. Many of these cases also exhibited marked

consistency, with the improvement with decreasing lead time coming primarily from error reductions in the more poorly performing cases. The results shown herein are meant to serve as a proof of concept and demonstrate the role that spatially averaged radar data, such as RDQVPs, polarimetric microphysical retrievals, and simple 1D models initialized from said retrievals could play in the operational nowcasting realm. Tools predicated on such an approach are envisioned as being complementary to existing nowcasting tools and observational analysis rather than a replacement but may offer better microphysical information and temporal resolution than can be provided by short-term model guidance at the expense of the spatial coverage afforded by such guidance. In addition to the goals discussed in section 4, future work will continue to explore other potential avenues of nowcasting informed by RDQVPs, such as increases in snowfall intensity preceded by K_{dp} signatures aloft.

Acknowledgments. Funding was provided by NOAA/Office of Oceanic and Atmospheric Research under NOAA–University of Oklahoma Cooperative Agreement NA16OAR4320115, U.S. Department of Commerce, as well as National Science Foundation Grant 1841246. The authors thank John Krause for assistance in generating the RDQVPs, Elizabeth Smith and Lee Dunnavan for insightful discussions, and Dana Tobin for helpful suggestions for the paper, as well as the three anonymous reviewers for their constructive feedback that greatly improved this article.

Data availability statement. All radar and RAP data used in this study are archived and freely available through the NOAA National Centers for Environmental Information (https://www.ncdc.noaa.gov/data-access). The ASOS observations used in this study are available from the Iowa Environmental Mesonet archive (https://mesonet.agron.iastate.edu/). Licensing for research (noncommercial) access to the mPING observations used in this study is available upon request (https://mping.ou.edu/static/mping/access.html).

REFERENCES

Andrić, J., M. R. Kumjian, D. S. Zrnić, J. M. Straka, and V. M. Melnikov, 2013: Polarimetric signatures above the melting layer in winter storms: An observational and modeling study. *J. Appl. Meteor. Climatol.*, **52**, 682–700, https://doi.org/10.1175/JAMC-D-12-028.1.

ASOS Program Office Staff, 1998: Automated Surface Observing System user's guide. National Weather Service ASOS Program Office Tech. Rep., 70 pp., https://www.weather.gov/media/asos/aum-toc.pdf.

Associated Press, 2013: Winter weather causes pile-ups, flight delays and leaves dangerous roads for Mid-Atlantic commuters. CBS News, 9 December 2013, https://www.cbsnews.com/news/winter-weather-snow-storm-mid-atlantic-commuters/.

Auria, R., and B. Campistron, 1987: Origin of precipitation and dynamic organization in wavelike precipitation bands. *J. Atmos. Sci.*, **44**, 3329–3340, https://doi.org/10.1175/1520-0469(1987)044<3329:OOPADO>2.0.CO;2.

Bacon, N., B. D. Swanson, M. B. Baker, and E. J. Davis, 1998: Breakup of levitated frost particles. *J. Geophys. Res.*, **103**, 13 763–13 775, https://doi.org/10.1029/98JD01162.

Bailey, M. P., and J. Hallett, 2009: A comprehensive habit diagram for atmospheric ice crystals: Confirmation from the laboratory, AIRS II, and other field studies. *J. Atmos. Sci.*, **66**, 2888–2899, https://doi.org/10.1175/2009JAS2883.1.

Bauer, P., A. Thorpe, and G. Brunet, 2015: The quiet revolution of numerical weather prediction. *Nature*, **525**, 47–55, https://doi.org/10.1038/nature14956.

Bechini, R., L. Baldini, and V. Chandrasekar, 2013: Polarimetric radar observations in the ice region of precipitation clouds at C-band and X-band radar frequencies. *J. Appl. Meteor. Climatol.*, **52**, 1147–1169, https://doi.org/10.1175/JAMC-D-12-055.1.

Benjamin, S. G., and Coauthors, 2016: A North American hourly assimilation and model forecast cycle: The Rapid Refresh. *Mon. Wea. Rev.*, **144**, 1669–1694, https://doi.org/10.1175/MWR-D-15-0242.1.

Black, A. W., and T. L. Mote, 2015a: Characteristics of winter-precipitation-related transportation fatalities in the United States. *Wea. Climate Soc.*, **7**, 133–145, https://doi.org/10.1175/WCAS-D-14-00011.1.

——, and ——, 2015b: Effects of winter precipitation on automobile collisions, injuries, and fatalities in the United States. *J. Transp. Geogr.*, **48**, 165–175, https://doi.org/10.1016/j.jtrangeo.2015.09.007.

Brandes, E. A., K. Ikeda, G. Zhang, M. Schönhuber, and R. M. Rasmussen, 2007: A statistical and physical description of hydrometeor distributions in Colorado snowstorms using a video disdrometer. *J. Appl. Meteor. Climatol.*, **46**, 634–650, https://doi.org/10.1175/JAM2489.1.

Bukovčić, P., A. Ryzhkov, D. Zrnić, and G. Zhang, 2018: Polarimetric radar relations for quantification of snow based on disdrometer data. *J. Appl. Meteor. Climatol.*, **57**, 103–120, https://doi.org/10.1175/JAMC-D-17-0090.1.

——, ——, and ——, 2020: Polarimetric relations for snow estimation—Radar verification. *J. Appl. Meteor. Climatol.*, **59**, 991–1009, https://doi.org/10.1175/JAMC-D-19-0140.1.

——, ——, and J. T. Carlin, 2021: Polarimetric relations for estimation of visibility in aggregated snow. *J. Atmos. Oceanic Technol.*, **35**, 805–822, https://doi.org/10.1175/JTECH-D-20-0088.1

Carlin, J. T., and A. V. Ryzhkov, 2019: Estimation of melting-layer cooling rate from dual-polarization radar: Spectral bin model simulations. *J. Appl. Meteor. Climatol.*, **58**, 1485–1508, https://doi.org/10.1175/JAMC-D-18-0343.1.

Clough, S. A., and R. A. A. Franks, 1991: The evaporation of frontal and other stratiform precipitation. *Quart. J. Roy. Meteor. Soc.*, **117**, 1057–1080, https://doi.org/10.1002/qj.49711750109.

——, H. W. Lean, N. M. Roberts, and R. M. Forbes, 2000: Dynamical effects of ice sublimation in a frontal wave. *Quart. J. Roy. Meteor. Soc.*, **126**, 2405–2434, https://doi.org/10.1002/qj.49712656804.

Dominé, F., T. Lauzier, A. Cabanes, L. Legagneux, W. F. Kuhs, K. Techmer, and T. Heinrichs, 2003: Snow metamorphism as revealed by scanning electron microscopy. *Microsc. Res. Tech.*, **62**, 33–48, https://doi.org/10.1002/jemt.10384.

Dong, Y., R. G. Oraltay, and J. Hallett, 1994: Ice particle generation during evaporation. *Atmos. Res.*, **32**, 45–53, https://doi.org/10.1016/0169-8095(94)90050-7.

Elmore, K. L., Z. L. Flamig, V. Lakshmanan, B. T. Kaney, V. Farmer, H. D. Reeves, and L. S. Rothfusz, 2014: mPING: Crowd-sourcing weather reports for research. *Bull. Amer. Meteor. Soc.*, **95**, 1335–1342, https://doi.org/10.1175/BAMS-D-13-00014.1.

Field, P. R., A. J. Heymsfield, A. Bansemer, and C. H. Twohy, 2008: Determination of the combined ventilation factor and capacitance for ice crystal aggregates from airborne observations in a tropical anvil cloud. *J. Atmos. Sci.*, **65**, 376–391, https://doi.org/10.1175/2007JAS2391.1.

Forbes, R. M., and R. J. Hogan, 2006: Observations of the depth of ice particle evaporation beneath frontal cloud to improve NWP modeling. *Quart. J. Roy. Meteor. Soc.*, **132**, 865–883, https://doi.org/10.1256/qj.04.187.

Frick, C., and H. Wernli, 2012: A case study of high-impact wet snowfall in northwest Germany (25–27 November 2005): Observations, dynamics, and forecast performance. *Wea. Forecasting*, **27**, 1217–1234, https://doi.org/10.1175/WAF-D-11-00084.1.

Gallus, W. A., and M. Segal, 1999: Diabatic effects on late-winter cold front evolution: Conceptual and numerical model evaluations. *Mon. Wea. Rev.*, **127**, 1518–1537, https://doi.org/10.1175/1520-0493(1999)127<1518:DEOLWC>2.0.CO;2.

Garrett, T. J., S. E. Yuter, C. Fallgatter, K. Shkurko, S. R. Rhodes, and J. L. Endries, 2015: Orientations and aspect ratios of falling snow. *Geophys. Res. Lett.*, **42**, 4617–4622, https://doi.org/10.1002/2015GL064040.

Giangrande, S. E., J. M. Krause, and A. V. Ryzhkov, 2008: Automatic designation of the melting layer with a polarimetric prototype of the WSR-88D radar. *J. Appl. Meteor. Climatol.*, **47**, 1354–1364, https://doi.org/10.1175/2007JAMC1634.1.

Grazioli, J., G. Lloyd, L. Panziera, C. R. Hoyle, P. J. Connolly, J. Henneberger, and A. Berne, 2015: Polarimetric radar and in situ observations of riming and snowfall microphysics during CLACE 2014. *Atmos. Chem. Phys.*, **15**, 13 787–13 802, https://doi.org/10.5194/acp-15-13787-2015.

Griffin, E. M., T. J. Schuur, and A. V. Ryzhkov, 2018: A polarimetric analysis of ice microphysical processes in snow, using quasi-vertical profiles. *J. Appl. Meteor. Climatol.*, **57**, 31–50, https://doi.org/10.1175/JAMC-D-17-0033.1.

——, ——, and ——, 2020: A polarimetric radar analysis of ice microphysical processes in melting layers of winter storms using S-band quasi-vertical profiles. *J. Appl. Meteor. Climatol.*, **59**, 751–767, https://doi.org/10.1175/JAMC-D-19-0128.1.

Hall, W. D., and H. R. Pruppacher, 1976: The survival of ice particles falling from cirrus clouds in subsaturated air. *J. Atmos. Sci.*, **33**, 1995–2006, https://doi.org/10.1175/1520-0469(1976)033<1995:TSOIPF>2.0.CO;2.

Harrington, J., K. Sulia, and H. Morrison, 2013: A method for adaptive habit prediction in bulk microphysical models. Part I: Theoretical development. *J. Atmos. Sci.*, **70**, 349–364, https://doi.org/10.1175/JAS-D-12-040.1.

Harris, F. I., 1977: The effects of evaporation at the base of ice precipitation layers: Theory and radar observations. *J. Atmos. Sci.*, **34**, 651–672, https://doi.org/10.1175/1520-0469(1977)034<0651:TEOEAT>2.0.CO;2.

Hendry, A., Y. M. M. Antar, and G. C. McCormick, 1987: On the relationship between the degree of preferred orientation in precipitation and dual-polarization radar echo characteristics. *Radio Sci.*, **22**, 37–50, https://doi.org/10.1029/RS022i001p00037.

Hogan, R. J., L. Tian, P. R. A. Brown, C. D. Westbrook, A. J. Heymsfield, and J. D. Eastment, 2012: Radar scattering from ice aggregates using the horizontally aligned oblate spheroid approximation. *J. Appl. Meteor. Climatol.*, **51**, 655–671, https://doi.org/10.1175/JAMC-D-11-074.1.

Homan, J., and L. W. Uccellini, 1987: Winter forecast problems associated with light to moderate snow events in the mid-Atlantic states on 14 and 22 February 1986. *Wea. Forecasting*, **2**, 206–228, https://doi.org/10.1175/1520-0434(1987)002<0206:WFPAWL>2.0.CO;2.

Jambon-Puillet, E., N. Shahidzadeh, and D. Bonn, 2018: Singular sublimation of ice and snow crystals. *Nat. Commun.*, **9**, 4191, https://doi.org/10.1038/s41467-018-06689-x.

Jiang, Z., J. Verlinde, E. E. Clothiaux, K. Aydin, and C. Schmitt, 2019: Shapes and fall orientations of ice particle aggregates. *J. Atmos. Sci.*, **76**, 1903–1916, https://doi.org/10.1175/JAS-D-18-0251.1.

Kain, J. S., S. M. Goss, and M. E. Baldwin, 2000: The melting effect as a factor in precipitation-type forecasting. *Wea. Forecasting*, **15**, 700–714, https://doi.org/10.1175/1520-0434(2000)015<0700:TMEAAF>2.0.CO;2.

Kantha, L., H. Luce, and H. Hashiguchi, 2019: Midlevel cloud-base turbulence: Radar observations and models. *J. Geophys. Res.*, **124**, 3223–3245, https://doi.org/10.1029/2018JD029479.

Kennedy, P. C., and S. A. Rutledge, 2011: S-band dual-polarization radar observations of winter storms. *J. Appl. Meteor. Climatol.*, **50**, 844–858, https://doi.org/10.1175/2010JAMC2558.1.

Klett, J. D., 1995: Orientation model for particles in turbulence. *J. Atmos. Sci.*, **52**, 2276–2285, https://doi.org/10.1175/1520-0469(1995)052<2276:OMFPIT>2.0.CO;2.

Korolev, A., and G. Isaac, 2003: Roundness and aspect ratio of particles in ice clouds. *J. Atmos. Sci.*, **60**, 1795–1808, https://doi.org/10.1175/1520-0469(2003)060<1795:RAAROP>2.0.CO;2.

——, ——, and J. Hallett, 1999: Ice particle habits in Arctic clouds. *Geophys. Res. Lett.*, **26**, 1299–1302, https://doi.org/10.1029/1999GL900232.

——, and Coauthors, 2017: Mixed-phase clouds: Progress and challenges. *Ice Formation and Evolution in Clouds and Precipitation: Measurement and Modeling Challenges*, *Meteor. Monogr.*, No. 58, Amer. Meteor. Soc., https://doi.org/10.1175/AMSMONOGRAPHS-D-17-0001.1.

——, and Coauthors, 2020: A new look at the environmental conditions favorable to secondary ice production. *Atmos. Chem. Phys.*, **20**, 1391–1429, https://doi.org/10.5194/acp-20-1391-2020.

Kudo, A., 2013: The generation of turbulence below midlevel cloud bases: The effect of cooling due to sublimation of snow. *J. Appl. Meteor. Climatol.*, **52**, 819–833, https://doi.org/10.1175/JAMC-D-12-0232.1.

——, H. Luce, H. Hashiguchi, and R. Wilson, 2015: Convective instability underneath midlevel clouds: Comparisons between numerical simulations and VHF radar observations. *J. Appl. Meteor. Climatol.*, **54**, 2217–2227, https://doi.org/10.1175/JAMC-D-15-0101.1.

Kumjian, M. R., and K. A. Lombardo, 2017: Insights into the evolving microphysical and kinematic structure of northeastern U.S. winter storms from dual-polarization Doppler radar. *Mon. Wea. Rev.*, **145**, 1033–1061, https://doi.org/10.1175/MWR-D-15-0451.1.

——, S. Mishra, S. E. Giangrande, T. Toto, A. V. Ryzhkov, and A. Bansemer, 2016: Polarimetric radar and aircraft observations of saggy bright bands during MC3E. *J. Geophys. Res.*, **121**, 3584–3607, https://doi.org/10.1002/2015JD024446.

——, D. M. Tobin, M. Oue, and P. Kollias, 2020: Microphysical insights into ice pellet formation revealed by fully polarimetric Ka-band Doppler radar. *J. Appl. Meteor. Climatol.*, **59**, 1557–1580, https://doi.org/10.1175/JAMC-D-20-0054.1.

Lazo, J. K., H. R. Hosterman, J. M. Sprague-Hilderbrand, and J. E. Adkins, 2020: Impact-based decision support services and the socioeconomic impacts of winter storms. *Bull. Amer. Meteor.*

Soc., **101**, E626–E639, https://doi.org/10.1175/BAMS-D-18-0153.1.

Leinonen, J., and W. Szyrmer, 2015: Radar signatures of snowflake riming: A modeling study. *Earth Space Sci.*, **2**, 346–358, https://doi.org/10.1002/2015EA000102.

Leroux, J., 2019: Guide to aircraft ground deicing. SAE Tech. Rep., 304 pp.

Leys, C., C. Ley, O. Klein, P. Bernard, and L. Licata, 2013: Detecting outliers: Do not use standard deviation around the mean, use absolute deviation around the median. *J. Exp. Soc. Psychol.*, **49**, 764–766, https://doi.org/10.1016/j.jesp.2013.03.013.

Li, H., D. Moisseev, and A. von Lerber, 2018: How does riming affect dual-polarization radar observations and snowflake shape? *J. Geophys. Res.*, **123**, 6070–6081, https://doi.org/10.1029/2017JD028186.

Lo, K. K., and R. E. Passarelli, 1982: The growth of snow in winter storms: An airborne observational study. *J. Atmos. Sci.*, **39**, 697–706, https://doi.org/10.1175/1520-0469(1982)039<0697:TGOSIW>2.0.CO;2.

Market, P. S., R. W. Przybylinski, and S. M. Rochette, 2006: The role of sublimational cooling in a late-season Midwestern snow event. *Wea. Forecasting*, **21**, 364–382, https://doi.org/10.1175/WAF919.1.

Maxwell Garnett, J. C., 1904: Color in metal glasses and in metallic films. *Philos. Trans. Roy. Soc.*, **203A**, 385–420, https://doi.org/10.1098/rsta.1904.0024.

McDonald, J. E., 1963: Use of the electrostatic analogy in studies of ice crystal growth. *Z. Angew. Math. Phys.*, **14**, 610–620, https://doi.org/10.1007/BF01601268.

Mills, B., J. Andrey, S. Doherty, B. Doberstein, and J. Yessis, 2020: Winter storms and fall-related injuries: Is it safer to walk than to drive? *Wea. Climate Soc.*, **12**, 421–434, https://doi.org/10.1175/WCAS-D-19-0099.1.

Mitra, S. K., O. Vohl, M. Ahr, and H. R. Pruppacher, 1990: A wind tunnel and theoretical study of the melting behavior of atmospheric ice particles. IV: Experiment and theory for snow flakes. *J. Atmos. Sci.*, **47**, 584–591, https://doi.org/10.1175/1520-0469(1990)047<0584:AWTATS>2.0.CO;2.

Mohney, G., 2013: Motorists stranded for hours after fatal 50-car car pile-up in Pa. ABC News, 8 December 2013, https://abcnews.go.com/US/motorists-stranded-hours-fatal-50-car-pile-pa/story?id=21143139.

Moisseev, D. M., S. Lautaportti, J. Tyynela, and S. Lim, 2015: Dual-polarization radar signatures in snowstorms: Role in snowflake aggregation. *J. Geophys. Res.*, **120**, 12 644–12 655, https://doi.org/10.1002/2015JD023884.

Murphy, A. M., A. Ryzhkov, and P. Zhang, 2020: Columnar vertical profile (CVP) methodology for validating polarimetric radar retrievals in ice using in situ aircraft measurements. *J. Atmos. Oceanic Technol.*, **37**, 1623–1642, https://doi.org/10.1175/JTECH-D-20-0011.1.

National Centers for Environmental Information, 2014: National climate report for December 2013. NOAA, accessed 4 May 2021, https://www.ncdc.noaa.gov/sotc/national/201312.

National Weather Service, 1996: Aviation weather observations for Supplementary Aviation Weather Reporting Stations (SAWRS). NWS Observing Handbook 8, 107 pp., https://www.weather.gov/media/surface/WSOH8.pdf.

Nelson, J., 1998: Sublimation of ice crystals. *J. Atmos. Sci.*, **55**, 910–919, https://doi.org/10.1175/1520-0469(1998)055<0910:SOIC>2.0.CO;2.

Oraltay, R. G., and J. Hallett, 1989: Evaporation and melting of ice crystals: A laboratory study. *Atmos. Res.*, **24**, 169–189, https://doi.org/10.1016/0169-8095(89)90044-6.

Parker, D. J., and A. J. Thorpe, 1995: The role of snow sublimation in frontogenesis. *Quart. J. Roy. Meteor. Soc.*, **121**, 763–782, https://doi.org/10.1002/qj.49712152403.

Pruppacher, H. R., and J. D. Klett, 1997: *Microphysics of Clouds and Precipitation.* 2nd ed. Kluwer Academic, 954 pp.

Qiu, L., and W. A. Nixon, 2008: Effects of adverse weather on traffic crashes: Systematic review and meta-analysis. *Transp. Res. Rec.*, **2055**, 139–146, https://doi.org/10.3141/2055-16.

Rasmussen, R. M., J. Vivekanandan, J. Cole, B. Myers, and C. Masters, 1999: The estimation of snowfall rate using visibility. *J. Appl. Meteor.*, **38**, 1542–1563, https://doi.org/10.1175/1520-0450(1999)038<1542:TEOSRU>2.0.CO;2.

Ryzhkov, A., and D. S. Zrnić, 2019: *Radar Polarimetry for Weather Observations.* Springer, 486 pp.

——, S. E. Giangrande, V. M. Melnikov, and T. J. Schuur, 2005: Calibration issues of dual-polarization radar measurements. *J. Atmos. Oceanic Technol.*, **22**, 1138–1155, https://doi.org/10.1175/JTECH1772.1.

——, M. Pinsky, A. Pokrovsky, and A. Khain, 2011: Polarimetric radar observation operator for a cloud model with spectral microphysics. *J. Appl. Meteor. Climatol.*, **50**, 873–894, https://doi.org/10.1175/2010JAMC2363.1.

Schneebeli, M., N. Dawes, M. Lehning, and A. Berne, 2013: High-resolution vertical profiles of X-band polarimetric radar observables during snowfall in the Swiss Alps. *J. Appl. Meteor. Climatol.*, **52**, 378–394, https://doi.org/10.1175/JAMC-D-12-015.1.

Schrom, R. S., and M. R. Kumjian, 2016: Connecting microphysical processes in Colorado winter storms with vertical profiles of radar observations. *J. Appl. Meteor. Climatol.*, **55**, 1771–1787, https://doi.org/10.1175/JAMC-D-15-0338.1.

——, and ——, 2018: Bulk-density representations of branched planar ice crystals: Errors in the polarimetric radar variables. *J. Appl. Meteor. Climatol.*, **57**, 333–346, https://doi.org/10.1175/JAMC-D-17-0114.1.

——, ——, and Y. Lu, 2015: Polarimetric radar signatures of dendritic growth zones within Colorado winter storms. *J. Appl. Meteor. Climatol.*, **54**, 2365–2388, https://doi.org/10.1175/JAMC-D-15-0004.1.

——, M. van Lier-Walqui, M. R. Kumjian, J. Y. Harrington, A. A. Jensen, and Y.-S. Chen, 2021: Radar-based Bayesian estimation of ice crystal growth parameters within a microphysical model. *J. Atmos. Sci.*, **78**, 549–569, https://doi.org/10.1175/JAS-D-20-0134.1.

Sinclair, V. A., D. Moisseev, and A. von Lerber, 2016: How dual-polarization radar observations can be used to verify model representation of secondary ice. *J. Geophys. Res.*, **121**, 10 954–10 970, https://doi.org/10.1002/2016JD025381.

Sulia, K. J., and J. Y. Harrington, 2011: Ice aspect ratio influences on mixed-phase clouds: Impacts on phase partitioning in parcel models. *J. Geophys. Res.*, **116**, D21309, https://doi.org/10.1029/2011JD016298.

——, and M. R. Kumjian, 2017: Simulated polarimetric fields of ice vapor growth using the adapative habit model. Part I: Large-eddy simulations. *Mon. Wea. Rev.*, **145**, 2281–2302, https://doi.org/10.1175/MWR-D-16-0061.1.

Szeto, K. K., and R. E. Stewart, 1997: Effects of melting on frontogenesis. *J. Atmos. Sci.*, **54**, 689–702, https://doi.org/10.1175/1520-0469(1997)054<0689:EOMOF>2.0.CO;2.

Tobin, D. M., and M. R. Kumjian, 2017: Polarimetric radar and surface-based precipitation-type observations of ice pellet to freezing rain transitions. *Wea. Forecasting*, **32**, 2065–2082, https://doi.org/10.1175/WAF-D-17-0054.1.

Trömel, S., A. V. Ryzhkov, P. Zhang, and C. Simmer, 2014: Investigations of backscatter differential phase in the melting layer. *J. Appl. Meteor. Climatol.*, **53**, 2344–2359, https://doi.org/10.1175/JAMC-D-14-0050.1.

——, ——, B. Hickman, K. Mühlbauer, and C. Simmer, 2019: Polarimetric radar variables in the layers of melting and dendritic growth at X band—Implications for a nowcasting strategy in stratiform rain. *J. Appl. Meteor. Climatol.*, **58**, 2497–2522, https://doi.org/10.1175/JAMC-D-19-0056.1.

Ulbrich, C. W., 1983: Natural variations in the analytical form of the raindrop size distribution. *J. Climate Appl. Meteor.*, **22**, 1764–1775, https://doi.org/10.1175/1520-0450(1983)022<1764:NVITAF>2.0.CO;2.

Voigtländer, J., and Coauthors, 2018: Surface roughness during depositional growth and sublimation of ice crystals. *Atmos. Chem. Phys.*, **18**, 13 687–13 702, https://doi.org/10.5194/acp-18-13687-2018.

Westbrook, C. D., A. J. Illingworth, E. J. O'Connor, and R. J. Hogan, 2010: Doppler lidar measurements of oriented planar ice crystals falling from supercooled and glaciated layer clouds. *Quart. J. Roy. Meteor. Soc.*, **136**, 260–276, https://doi.org/10.1002/qj.528.

Wexler, R., R. J. Reed, and J. Honig, 1954: Atmospheric cooling by melting snow. *Bull. Amer. Meteor. Soc.*, **35**, 48–51, https://doi.org/10.1175/1520-0477-35.2.48.

Wilks, D. S., 2011: *Statistical Methods in the Atmospheric Sciences.* 3rd ed. Elsevier, 676 pp.

Wolfensberger, D., D. Scipion, and A. Berne, 2016: Detection and characterization of the melting layer based on polarimetric radar scans. *Quart. J. Roy. Meteor. Soc.*, **142**, 108–124, https://doi.org/10.1002/qj.2672.